Modeling and Correction of Protein Conformational Disease in iPSC-derived Neurons through Personalized Base Editing

Colin T Konishi[1,2], Nancy Moulayes[1,2], Tanvi Butola[3], Vincent Zhang[1,2], Dana Kagan[1,2], Qiaoyan Yang[1,2], Mariel Pressler[1,4], Brooke G Dirvin[1,2], Orrin Devinsky[4,†], Jayeeta Basu[3†], Chengzu Long[1,2,3,4,†]

[1] NYU Cardiovascular Research Center, NYU Grossman School of Medicine, New York, NY 100016,

[2] Leon H. Charney Division of Cardiology, NYU Grossman School of Medicine, New York, NY 100016,

[3] Department of Neuroscience and Physiology, NYU Grossman School of Medicine, New York, NY 100016,

[4] Department of Neurology, NYU Grossman School of Medicine, New York, NY 100016.

† Corresponding authors:

E-mail: chengzu.long@nyumc.org (C.L.), Jayeeta.Basu@nyulangone.org (J.B.) and od4@nyu.edu (O.D.)

Base editing correction in conformational disease

Abstract

Altered protein conformation can cause incurable neurodegenerative disorders. Mutations in *SERPINI1*, the gene encoding neuroserpin, alter protein conformation resulting in cytotoxic aggregation in neuronal endoplasmic reticulum. Aggregates cause oxidative stress impairing function, leading to neuronal death. Familial encephalopathy with neuroserpin inclusion bodies (FENIB) is a rare autosomal dominant progressive myoclonic epilepsy. Patients present with seizures and cognitive impairments that progress to dementia and premature death. We developed HEK293T and induced pluripotent stem cell (iPSC) models of FENIB, harboring the patient's pathogenic *SERPINI1* variant or stably overexpressing mutant neuroserpin fused to GFP (MUT NS-GFP). FENIB cells form neuroserpin inclusions which increase in size and number. Here, we utilized a personalized adenine base editor (ABE)-mediated approach to efficiently correct the pathogenic variant and to restore neuronal dendritic morphology. ABE-treated MUT NS-GFP cells demonstrated reduced inclusion size and number. Using an inducible MUT NS-GFP neuron system, we identified early prevention of toxic protein expression allowed aggregate clearance, while late prevention halted neuronal impairments. To address several challenges for clinical applications of gene correction, we developed a neuron-specific engineered virus-like particle to optimize neuronal ABE delivery. Preventing mutant protein with altered conformation production improved toxic protein clearance. Our findings provide a targeted strategy and may treat FENIB and potentially other neurodegenerative diseases due to altered protein conformation such as Alzheimer's and Huntington's diseases.

Introduction

Altered protein conformation can cause progressive and incurable neurodegenerative disorders such as Alzheimer's and Huntington's diseases. [1,2] Neuroserpin (NS) is a serine protease inhibitor involved in neuronal axon growth and synapse formation. [3,4] Some mutations in the *SERPINI1* gene alter neuroserpin protein conformation, leading to polymerization within the endoplasmic reticulum (ER), causing ER and oxidative stress, neuronal dysfunction, and cell death.[5–7] Familial encephalopathy with neuroserpin inclusion bodies (FENIB) is a rare autosomal dominant progressive myoclonic epilepsy, causing seizures, dementia, motor impairments, and premature death.[8,9] The variant, *SERPINI1* c.1175 G>A (p.Gly392Glu) causes one of the most severe form of FENIB, characterized by absence seizures, myoclonic and tonic-clonic seizures, and progressive dementia begin in late childhood to early adolescence.[9,10] There are no disease-modifying therapies.[11,12]

Many clinical and preclinical strategies for treatment of conformational diseases, including Alzheimer's and Huntington's diseases, aim to reduce or eliminate expression of precursor forms of aggregation-prone proteins.[13,14] These strategies employ RNAi, antisense oligonucleotide, small molecular modulators, genome editors (e.g., zinc-fingers, TALENs and clustered regularly interspace palindromic repeat (CRISPR)/CRISPR-associated sequence (Cas) nucleases) to target pathogenic forms of RNA and DNA.[15–18] All approaches face their own challenges.

CRISPR/Cas genome editors are sequence-specific RNA-guided nucleases that generate double-strand breaks (DSB) in target DNA.[19–21] DSB repair through non-homologous end joining facilitates gene disruption by the formation of insertions and deletions, while homology directed repair (HDR) produces sequence-specific modifications by introducing an exogenous repair template.[22,23] Cas9 can edit stable cell lines and induced pluripotent stem cells (iPSCs) *in vitro* and neurons, cardiomyocytes, liver, and other cell types *in vivo*.[24–26] Advances in iPSC technology and CRISPR/Cas gene editing have led to the generation of novel isogenic cells harboring patient-

specific disease-causing variants.[27,28] These human iPSCs can be differentiated into FENIB neurons to model disease.[29] However, HDR is limited in therapeutic applications due to the cytotoxicity of DSBs and insertion or deletion (indel) mutations. [30] Furthermore, HDR does not work in post-mitotic cells including neurons. [31,32] Adenine base editing (ABE), a CRISPR/Cas9 modality, uses an evolved transfer RNA deaminase (tadA) fused to Cas9 nickase (nCas9) to act on single-stranded DNA, converting adenine (A) to guanosine (G) without a DSB. ABEs can generate precise A>G transition mutations to correct the pathogenic *SERPINI1* c.1175 G>A mutation.[33] ABEs work both *in vitro* and *in vivo*.

Engineered virus-like particles (eVLPs) target tissues with far fewer immunogenic effects and shorter expression then adeno-associated viruses (AAVs), thereby reducing off-target edits.[34–36] eVLPs are an extracellular vesicle formed of viral protein assemblies that can deliver cargo fused to retroviral Gag protein but do contain viral genomes. Fusion of ABE ribonucleoprotein to Moloney murine leukemia virus (MMLV) Gag protein enables direct delivery of editor without viral RNA, overcoming genomic packaging limits of common viral delivery, e.g. lentivirus and AAVs.[36] Further, eVLPs can target cell-types by modulating surface glycoprotein.[34] However, the efficiency of eVLP-delivered ABEs to correct mutations in cortical neurons remains unknown, as neurons use nonclassical nuclear import, partly due to reduced importin α1 expression, which recognizes classical nuclear localization signals.[37]

In this proof-of-concept study, for the first time, we generated endogenous knock-in (KI) and stable overexpression models of FENIB in HEK293T, and iPSC-derived neurons. We used ABEs to target and correct the pathogenic variant. Correction of the variant restored dendritic morphology in KI neurons, and clearance of NS-GFP aggregates in HEK293Ts. Using our inducible system, early treatment of NS-GFP neurons cleared aggregated protein, while later treatment prevented disease progression. We tested neuronal specific eVLPs with neuron specific nuclear localization signals (NLS) and identified improved neuronal editing. eVLP-mediated ABE

editing appears to be a safe and efficient treatment for FENIB, and potentially other diseases of protein conformation (e.g., Alzheimer's and Huntington's diseases).

Results

CRISPR/Cas9 mediated HDR KI of patient-specific *SERPINI1* variant.

The autosomal dominant *SERPINI1* c.1175 G>A (p. G392E) variant causes neuroserpin to form cytotoxic aggregates (**Fig. 1A, B**) .[9] To investigate ABE correction to treat this variant, we first generated a *SERPINI1* c.1175 G>A cell line using CRISPR/Cas9 mediated HDR to knock-in the variant in human embryonic kidney (HEK293T) cells. We tested SpCas9 and SpCas9-NG editors to target *SERPINI1* exon 9 (**Fig. 1B**).[38] Single guide RNAs (gRNA) were cloned into plasmids encoding SpCas9-2A-GFP (g1) or NG-SpCas9-2A-GFP (g2). g1 and g2 cleave *SERPINI1* proximal to c.1175, using a single stranded oligodeoxynucleotide donor (ssODN) to template DSB repair. g1 used a 5'-GGG-3' PAM located at *SERPINI1* c.1173-c.1175. KI of *SERPINI1* c.1175 G>A alters the PAM sequence to 5'-GG<u>A</u>-3', preventing recutting by SpCas9, to increase KI efficiency**.** g2 used a 5'-TG-3' PAM to generate a DSB immediately downstream of KI sequence to optimize HDR-mediated KI efficiency.[39] HEK293T cells were transfected using lipofectamine 2000 with g1 or g2 plasmids (**Fig. S1A, B**). 72-hours post-transfection, cells were sorted by GFP expression, and gRNA efficiency was measured by PCR-based T7 endonuclease I (T7E1) assay, Sanger sequencing and Synthego Inference of CRISPR Edits (Synthego ICE) analysis tool.[40] g1 and g2 demonstrated high editing activity. Next, we nucleofected HEK293T cells with g1 or g2 plasmids and *SERPINI1* c.1175 G>A ssODN for templated KI using the Lonza nucleofection SF system (**Fig. S1C**). 72-hours post-nucleofection we sorted GFP-positive cells into bulk populations or single cells to assess editing efficiencies and selected clones harboring the patient-specific *SERPINI1* c.1175 G>A variant. ICE identified modest HDR efficiencies by g1 (16.5%) and g2 (11.5%) (**Fig. S1D**). We used g2 to obtain fewer nonspecific indels.

We nucleofected iPSCs with either g1 or g2 plasmid and *SERPINI1* c.1175 G>A ssODN for templated KI. We identified 24% KI and 21% KI efficiency, consistent with our HEK293T edits (**Fig. S1D**). Although all FENIB patients carry heterozygous *SERPINI1* mutations, we assessed the impact of gene dosage on toxic gain-of-function aggregation or causing loss-of-function.[41] We selected heterozygous *SERPINI1* c.1175 G>A/+ (heterozygous KI) and homozygous *SERPINI1* c.1175 G>A/G>A (homozygous KI) clones with the patient-specific variant. Patient-specific iPSCs and isogenic control wildtype clones were clonally expanded for experiments.

Stable overexpression of GFP fused neuroserpin in human cells.

Cultured cell lines or mouse primary neural progenitors and neurons overexpressing neuroserpin protein can model FENIB.[12,42] We overexpressed neuroserpin to complement analysis of human *SERPINI1* KI iPSCs. Our approach using overexpression and KI of FENIB mutations in human iPSCs enables disease modeling and correction in 6-week-old in vitro neural cultures which more accurately recapitulates patient disease. We designed a lentivirus vector expressing wild-type (WT) or mutant (MUT) neuroserpin protein fused to enhanced green fluorescent protein (NS-GFP) under a constitutive CMV, or doxycycline inducible TRE, promoter (**Fig. 1C**). We transduced HEK293T cells with TRE-NS-GFP and reverse tetracycline-controlled transactivator (rtTA) lentivirus. The day after transduction, we induced NS-GFP expression by adding doxycycline to the media. The day after NS-GFP induction, cells expressed NS-GFP with no differences between WT and MUT NS-GFP cells' expression. By day 4, aggregation occurred in MUT NS-GFP cells. By day 7, MUT NS-GFP aggregates increased in size and number (**Fig. 1C**). Protein conformation in NS-GFP cells was confirmed using denaturing sodium dodecyl-sulfate polyacrylamide gel electrophoresis (SDS-PAGE) and nondenaturing native-PAGE immunoblotting (**Fig. 1D and Fig. S1E**). Immunoblot of SDS-PAGE using anti-neuroserpin or anti-GFP antibodies revealed a band of ~85kDa in the WT and MUT NS-GFP lanes; the combined weights of neuroserpin (55kDa) and GFP (30kDa) fusion protein. Native-PAGE immunoblots of WT and MUT NS-GFP confirmed NS-

GFP aggregation through fluorescent microscopy. WT NS-GFP revealed a single dominant band indicative of NS-GFP monomers when probing with anti-neuroserpin or anti-GFP antibodies. MUT NS-GFP had the same monomer band as WT NS-GFP in addition to banding and smearing at higher molecular weights, reflecting mutant NS-GFP aggregate polymers.

Neuroserpin aggregation in the endoplasmic reticulum (ER) causes ER stress mediated through the unfolded protein response (UPR) and ER overload response (EROR)[42,43]. We collected RNA from WT and MUT NS-GFP HEK293Ts, control cells stably expressing GFP, and control cells without any form of overexpression. We assessed ER stress through quantitative PCR (qPCR) of UPR response genes *BiP* and spliced *XBP1* (**Fig. S1F**). When normalized to control HEK293Ts, cells overexpressing GFP show no difference in fold expression. We find that both WT and MUT NS-GFP overexpressing cells reveal a significant fold increase in both *BiP* (WT NS-GFP: 4.1, MUT NS-GFP: 7.8, $p<0.0001$) and *sXBP1* (WT NS-GFP: 2.8, MUT NS-GFP: 3.9, $p<0.0001$), with the greatest increase in MUT NS-GFP expressing cells when normalized to *18s* transcript expression. Previous studies of cell metabolic activity have found that overexpression of WT NS reduces cellular viability[12]. In all, our immunofluorescent microscopy, native-PAGE immunoblot, and transcript analyses demonstrated stable overexpression of NS-GFP results in FENIB neuroserpin aggregation in human cells.

Generation of patient-specific iPSC-derived neurons through *Neurogenin2* induction.

To evaluate our iPSC *in vitro* FENIB phenotype model, we differentiated iPSCs into excitatory cortical neurons by overexpressing *Neurogenin2* (Ngn2) (**Fig. 1E**).[29] We assessed induction efficiency through immunocytochemical labeling of iPSCs before and 21 days (d21) after induction. iPSCs were labeled with pluripotency markers stage-specific embryonic antigen 4 (SSEA4) and SRY-Box transcription factor 2 (SOX2). iPSC-derived neurons (iNs) were labeled with neuron-specific microtubule associated protein-2 (MAP2), and synapse protein synapsin-1

(SYN1) (**Fig. 1E**). At d35, iNs also expressed neurofilament heavy (NFH) and neuronal nuclear protein (NeuN), characteristic of mature neurons (**Fig. S2A**).

Next, we sought to confirm the identity of our cells by comparing intrasample differential transcript expression in day 35 iPSC-derived neurons against previously published datasets (**Fig. S2B**).[29,44] We collected RNA from three independent inductions per genotype and performed polyA selected bulk RNA-seq to target mRNAs. Transcriptional profiles of d35 neurons revealed an enrichment of genes confirming neuronal identity. In a comparison to the Zhang 2013 dataset, we identified pan neuronal (*DCX*, *MAP2*, *TUBB3*), glutamate related (*SLC17A6*), and post-synaptic (*DLG4*) genes within our top five hits. Similarly, comparing against the Lindhout 2020 dataset, we see further enrichment for axon (*GAP43*, *BASP1*), and neuron (*STMN1*, *ENO2*, *SYP*) genes. Our immunocytochemical and transcriptomic analyses together confirm the neural identity of Ngn2 induced neurons.

Electrophysiology of iPSC-derived neuron model of FENIB.

We assessed physiological function in iPSC-derived neurons with evoked action potentials (AP) using whole-cell patch-clamp recordings in current clamp mode (**Fig. S3A-G**). While single APs were elicited in all neurons by day 14, with a burst of firing in a subset of tested cells, further maturation of the iNs till after day 42 elicited prototypical APs consistently across all cells recorded. Hence, we assessed day 42-44 iNs for intrinsic excitability.

No significant differences were observed between WT, HET. KI, and HOM. KI groups in AP rheobase (WT: 29.7±2.1 pA n=54, HET.KI: 25.4±1.6 pA n=46, HOM.KI: 28.1±2.0 pA n=47, $p>0.05$), full-width at half-maxima (WT: 2.0±0.1 ms n=52, HET. KI: 2.0±0.1 ms n=46, HOM. KI: 2.0±0.1 ms n=47, $p>0.05$), amplitude (WT: 84.7±1.2 mV n=52, HET. KI: 82.5±1.5 mV n=46, HOM. KI: 84.6±1.2 mV n=47, $p>0.05$), firing threshold (WT: -46.2 mV±1.1 n=52, HET. KI: -48.5±1.2 mV n=46, HOM. KI:-47.9±1.3 mV n=47 $p>0.05$), cell-capacitance (WT: 15.7±0.7 pF n=53, HET.KI:

15.5±0.6 pF n=46, HOM.KI: 16.5±0.7 pF n=49, p>0.05), and resting membrane potential (WT: -49.9±1.3 mV n=54, HET.KI: -49.5±1.3 mV n=45, HOM.KI: -49.9 mV±1.6 n=50, p>0.05). Our evoked AP findings were consistent with *in vitro* cortical neurons, validating our human neuronal model of FENIB.[45–47]

Characterizing neuroserpin inclusion bodies in NS-GFP overexpression iPSC-derived neuron FENIB model.

We hypothesized that preventing mutant neuroserpin production would facilitate clearance of aggregated protein (**Fig. 2A**).[48] To test this, we transduced iPSCs with ptetON NS-GFP lentivirus in addition to Ngn2 and rtTA lentivirus for inducing neuronal fate. Triply transduced cells were selected for following doxycycline induction using puromycin and blasticidin, with resistance conferred from Ngn2-T2A-PURO and NS-GFP-T2A-BSD lentivirus respectively.

NS-GFP expression was induced in cells, with observable protein one day after induction. By day 4, NS-GFP aggregates began forming in MUT NS-GFP cells. We hypothesized that early termination of mutant protein expression would facilitate protein clearance. We induced expression of NS-GFP for 6 days. Beginning on day 7, we separated cells into continued expression (+DOX) or discontinued expression through doxycycline withdrawal (W/D) until day 10 (**Fig. 2A**). Aggregated MUT NS-GFP signal is brighter than diffuse WT NS-GFP (**Fig. 2B**). Using ImageJ image analysis software, we set a fluorescence intensity threshold for GFP expression to quantify NS-GFP aggregate count and area and normalized these values to neuronal marker, NeuN, and 4'6-diamidino-2-phenylindole (DAPI) expression to normalize per neuron. We visualized cells with confocal microscopy to identify aggregate formation and clearance (**Fig. 2B-D**). Doxycycline withdrawal significantly reduced aggregate count per neuron (+DOX MUT NS-GFP: 0.73 aggregates/neuron, W/D MUT NS-GFP: 0.04 aggregates/neuron, p<0.0001) with W/D MUT NS-GFP values similar to control (ctrl) and WT NS-GFP aggregate counts (+DOX ctrl: 0, W/D ctrl: 0, +DOX WT NS-GFP: 0.02, W/D WT NS-GFP: 0, p>0.99) (**Fig.**

2C). Aggregate clearance was also reflected in aggregate area per neuron (+DOX MUT NS-GFP: 3.29 μm^2 /neuron, W/D MUT NS-GFP: 0.02 μm^2 aggregates/neuron, $p<0.01$) (**Fig. 2D**). Aggregate area per neuron in W/D MUT NS-GFP was restored to control levels (+DOX ctrl: 0 μm^2 /neuron, W/D ctrl: 0 μm^2 /neuron, +DOX WT NS-GFP: 0.004 μm^2/neuron, W/D WT NS-GFP: 0, $p>0.99$). Based off these findings, early termination of mutant NS expression is sufficient for the clearance of aggregating protein.

Next, we assessed if prolonged aggregate accumulation could be cleared by more mature neurons (**Fig. 2E-G**). We induced aggregation until day 21, then split samples and used confocal microscopy to visualize and assess per neuron aggregation count and area at days 21, 28(+DOX and W/D), and 35 (+DOX and W/D) (**Fig. 2A, 2E**). day 21 to day 28 aggregate count remained similar. Although W/D day 28 neurons trended towards fewer aggregates, aggregate count between day 21, +DOX day 28, and W/D day 28 neurons were not statistically significant (day 21: 0.82 aggregates/neuron, +DOX day 28: 0.71 aggregates/neuron, W/D day 28: 0.62 aggregates/neuron, $p>0.05$) (**Fig. 2F**). When we terminate expression at day 21 and assessed clearance in d35 neurons, W/D neurons showed a significant difference in aggregate count compared to +DOX counterparts (+DOX d35: 1.24 aggregates/neuron, W/D d35: 0.75 aggregates/neuron, $p<0.01$). W/D day 35 neuron aggregates/neuron values were similar to day 21 and day 28 neurons ($p>0.05$). Next, we assessed aggregate area by neuron, we identified a similar result. W/D Day 35 neurons had significantly reduced aggregate area per neuron compared to +DOX neurons (+DOX day 35: 3.2 μm^2/neuron, W/D day 35: 1.1 μm^2/neuron, $p<0.0001$) (**Fig. 2G**). This significant reduction was similar in area to day 21 and day 28 neurons (day 21: 1.427 μm^2/neuron, +DOX day 28:1.16 μm^2/neuron, W/D day 28: 0.89 μm^2/neuron, $p>0.05$). Thus, preventing MUT NS-GFP expression at day 21, and allowing toxic protein resolution until day 35 was insufficient to clear aggregates, but halted further aggregation. These doxycycline inducible NS-GFP studies suggested that early cessation of protein aggregation

allowed for complete aggregation clearance. By contrast, late-stage cessation prevented further aggregate accumulation.

iPSC-derived neurons overexpressing MUT NS-GFP show changes in membrane excitability.

We next assessed neuronal excitability and physiological function using whole cell patch clamp in current clamp mode to evoke APs in NS-GFP iNs (**Fig. S4A-G**). Based on the maturation of neurons at day 42 (**Fig. S3**), NS-GFP iNs at d42 were assessed for intrinsic properties of excitability including APs rheobase, full-width at half-maxima, amplitude, firing threshold, cell capacitance, and resting membrane potential. +DOX MUT NS-GFP neurons had increased rheobase compared to the WT NS-GFP counterparts (+DOX MUT NS-GFP: 73.1±14.3 pA n=8, +DOX WT MUT NS-GFP: 37.5±5.9 n=8, $p<0.05$) **(Fig. S4B)**. This suggests a decrease in membrane excitability consistent with other reports of protein aggregation based neurodegenerative disease models. [49,50] W/D d42 MUT NS-GFP (51.4±5.1 pA n=7) neurons had similar rheobase as WT NS-GFP (+DOX WT NS-GFP: 37.5±5.9 pA n=8, and W/D WT NS-GFP: 48.6±7.0 pA n=7, $p>0.05$) and control (+DOX CTRL: 52.5±4.5 pA n=8, and W/D CTRL: 63.3±8.2 n=9, $p>0.05$) neurons indicating that alteration to rheobase was rescued following termination of MUT NS-GFP expression. AP full-width at half-maxima (+DOX CTRL: 1.6±0.2 ms n=8, +DOX WT NS-GFP: 1.6±0.1 ms n=8, +DOX MUT NS-GFP: 1.4±0.1 ms n=8, W/D CTRL: 1.8±0.2 ms n=9, W/D WT NS-GFP: 1.7±0.2 ms n=7, W/D MUT NS-GFP: 1.6±0.1 ms n=7, $p>0.05$), amplitude (+DOX CTRL: 87.0±2.8 mV n=8, +DOX WT NS-GFP: 85.3±3.3 mV n=8, +DOX MUT NS-GFP: 84.3±2.0 mV n=8, W/D CTRL: 91.3±2.2 mV n=9, W/D WT NS-GFP: 85.6±0.8 mV n=7, W/D MUT NS-GFP: 88.0±3.6 mV n=7, $p>0.05$), firing threshold (+DOX CTRL: -49.0±2.7 mV n=8, +DOX WT NS-GFP: -52.3±1.6 mV n=8, +DOX MUT NS-GFP: -44.3.3±2.9 mV n=8, W/D CTRL: -49.1±2.7 mV n=9, W/D WT NS-GFP: -46.2±2.8 mV n=7, W/D MUT NS-GFP: -48.8±3.1 n=7, $p>0.05$), cell capacitance (+DOX CTRL: 30.2±3.9 pF n=8, +DOX WT NS-GFP: 24.4±1.6 pF n=8, +DOX MUT

NS-GFP: 26.1±2.9 pF n=7, W/D CTRL: 27.2±3.2 pF n=9, W/D WT NS-GFP: 24.0±2.7 pF n=8, W/D MUT NS-GFP: 29.8±4.2 pFn=6, p>0.05), and resting membrane potential (+DOX CTRL: -54.1±2.1 mV n=11, +DOX WT NS-GFP: -54.2±4.7 mV n=6, +DOX MUT NS-GFP: -56.6±2.9 n=7, W/D CTRL: -59.5±2.5 mV n=8, W/D WT NS-GFP: -57.6±5.0 mV n=8, W/D MUT NS-GFP: -61.9±3.3 n=9, p>0.05) were all similar. Our results demonstrate that neurons MUT NS-GFP have dysfunctional membrane excitability, which is rescued once MUT NS-GFP expression is terminated.

ABE-mediated correction of *SERPINI1* c.1175 G>A variant.

We studied ABEs correction of c.1175 G>A to the WT sequence. We identified a shortened 5'-NG-3' PAM sequence downstream of the patient variant, recognized by ABEs built on NG-SpCas9 editor, to position the variant within the editing window at the A5 position (**Fig. 3A**). Rationally designed and evolved ABE variants can increase editing efficiency and reduce off-target effects.[51–53] We tested four ABEs to identify optimal editing at the *SERPINI1* c.1175 locus. We subcloned the NG-SpCas9 into four next-generation ABEs resulting in NG-ABEmax, NG-SECURE-miniABEmax-V82G (NG-V82G), NG-SECURE-miniABEmax-K20AR21A (NG-K20AR21A), and NG-ABE8e.[52,54,55] We found a candidate bystander mutation within the editing window at the A6 position. We hypothesized that this bystander mutation would be tolerated due to its location at the codon wobble position. Combination target and bystander editing encodes the wild-type residue (G, glycine), while bystander-only editing would not alter the pathogenic residue (E, glutamic acid).

We cloned a mutant-specific sgRNA into the plasmid, pBSU6-sgRNA-GFP (g3), which was nucleofected with a plasmid encoding ABE using the Lonza P3 nucleofection system in homozygous KI iPSCs. EditR Sanger sequencing trace analysis and deep sequencing assessed ABE correction efficiency.[56] EditR analysis revealed NG-ABE8e (A:T to G:C conversion efficiency, ~86%) and NG-ABEmax (48%) had the greatest correction efficiency, with modest editing by NG-

V82G (16%) and NG-K20AR21A (13%) (**Fig. 3B**). After Sanger sequencing, we deep sequenced homozygous KI iPSCs treated with the two most efficient ABEs, NG-ABEmax and NG-ABE8e (**Fig. 3C**). Deep sequencing reads revealed codon specific editing outcomes with NG-ABEmax encoding 75% wild-type glycine (GGA or GGG) and NG-ABE8e encoding 92% glycine. NG-ABEmax activity resulted in more reversion to wild-type codon (GGA: 62%, GGG: 13%) while NG-ABE8e had more codons harboring the permissive bystander mutation (GGA: 35%, GGG: 57%).

We treated MUT NS-GFP iPSCs with plasmids encoding g3 and NG-ABE8e (see above) to assess if NG-ABE8e editing could correct MUT NS-GFP iPSCs (**Fig. 3D**). EditR base calling analysis of Sanger sequencing traces revealed (~90%editing in homozygous iPSCs and ~65% in MUT NS-GFP iPSCs. Thus, NG-ABE8e with g3 can efficiently correct the endogenous loci with relevant genomic context in homozygous KI cells, and the MUT NS-GFP stably incorporated models of FENIB.

ABE correction of MUT NS-GFP in HEK293T cells allows aggregate clearance.

We evaluated ABE treatment on NS aggregate clearance. Using lentivirus transduction, we stably incorporated either WT or MUT NS-GFP constitutively expressed under the CMV promoter into HEK293T cells. Following the observation of GFP expression, we sorted single cells for independent biological replicates.

Constitutively expressing MUT NS-GFP HEK293T cells were transfected with NG-ABE8e-T2A-tagRFP and g3 plasmids co-expressing tagRFP (ABE+g3), or NG-ABE8e-T2A-tagRFP only (ABE only) as control. 72-hours post-transfection, GFP+/RFP+ double positive cells were collected to assess DNA correction and NS-GFP aggregate clearance. EditR analysis revealed ~80% correction of the variant to the WT sequence in ABE+g3 MUT NS-GFP cells (**Fig. 4A**). Immunoblotting whole cell lysate from ABE+g3 MUT NS-GFP and control HEK293Ts revealed similar levels of NS-GFP protein expression when probed with anti-neuroserpin antibody (**Fig.**

4B). We sought to visualize NS-GFP expression and aggregation using confocal microscopy in ABE+g3 MUT NS-GFP cells (**Fig. 4C**). We determined total cells per imaging field to assess for culturing fitness differences and did not identify any statistically significant changes (WT NS-GFP: 275 cells, ABE only MUT NS-GFP: 256 cells, ABE+g3 MUT NS-GFP: 272 cells, $p>0.05$) (**Fig. 4D**).

Next, we assessed the effects of ABE+g3 treatment of MUT NS-GFP cells on NS-GFP aggregation (**Fig. 4E and 4F**). ABE+g3 MUT NS-GFP cells had significantly reduced aggregates per cell compared to ABE only MUT NS-GFP cells (ABE only MUT NS-GFP: 1.49 aggregates/cell, ABE+g3 MUT NS-GFP: 0.58 aggregates/cell, $p<0.0001$) (**Fig. 4E**). Although ABE+g3 treatment significantly reduced aggregates per cell, there was still a significant difference in aggregates per cell when compared to WT NS-GFP (WT NS-GFP: 0.10 aggregates/cell, $p<0.05$). As ABE+g3 MUT NS-GFP cells are a mosaic of 80% corrected 20% variant sequence NS-GFP, we rationalized that aggregate count would reflect the DNA level mosaicism. ABE+g3 MUT NS-GFP cells had significantly reduced NS-GFP aggregate area per cell compared to ABE only (ABE only MUT NS-GFP: 2.94 μm^2/cell, ABE+g3 MUT NS-GFP: 0.83 μm^2/cell, $p<0.01$) (**Fig. 4F**). Despite the heterogeneity of ABE correction, ABE+g3 treatment was sufficient to restore aggregate area per cell value back to WT NS-GFP (WT NS-GFP: 0.20 μm^2/cell, $p>0.05$). Based off our results, we conclude that ABEs can correct the FENIB mutation and allow aggregate clearance.

Impaired dendritic arborization in heterozygous and homozygous KI iPSC-derived neurons is corrected with ABE treatment.

Neuroserpin is expressed during late stage neuronal maturation with roles in dendritic morphology, synaptic maturation, and neuronal differentiation.[57–59] Cultured rat hippocampal neurons overexpressing neuroserpin have increased dendritic arborization and altered spine shapes.[58] *In vivo* analysis of neuroserpin-deficient mice revealed a decrease in spine-synapses.[60] We evaluated whether dendritic morphology was affected in heterozygous and homozygous KI

neurons, and whether ABE corrected neurons showed restored morphology **(Fig. 5A)**. We transfected d35 WT, heterozygous KI, homozygous KI, and ABE corrected neurons with GFP expressing plasmids for 30 minutes to sparsely label single cells. 24-hours post-transfection, we fixed coverslips for staining with anti-GFP antibodies to increase signal in imaging for Sholl analysis. Using ImageJ, we set a fluorescence intensity threshold against GFP expression to image the morphology of single neurons. Then using Simple Neurite Tracer (SNT), we assessed the number of dendritic intersections at 10 μm radial distances from the neuron soma **(Fig. 5B).**[61,62]

We observed no significant differences in intersection numbers between WT, heterozygous KI, homozygous KI, and ABE corrected neurons at d35 for any radial distance from soma. Intersection numbers peaked at 20 μm for WT (~9.6 dendrites), heterozygous KI (~9 dendrites), and ABE corrected (~7.3 dendrites) and at 30 μm for homozygous KI (~8.6 dendrites) (**Fig. 5C**). Based off the number of intersections at radial distances, we calculated area under the curve (AUC) to determine overall dendritic arborization (**Fig. 5D**). Although WT and ABE corrected neurons appeared to have slightly greater AUC than both KI groups, statistical testing reveal no significant difference (WT: 819 arbitrary units (AU), heterozygous KI: 752 AU, homozygous KI: 620 AU, ABE corrected: 853 AU, $p>0.05$). Similarly, we quantified total dendritic length and found no statistically significant differences (WT: 1022.2 μm, heterozygous KI: 938.4 μm, homozygous KI: 864.4 μm, ABE corrected: 1177.5 μm, $p>0.05$) (**Fig. 5E**).

As neuroserpin functions in late-stage neuronal maturation, we allowed further neuronal development and assessed dendritic morphology again at d42 (**Fig. 5F-H)**. Intersection number peaked at 30 μm for WT (~11.6 dendrites), homozygous KI (~7.9 dendrites), and ABE corrected neurons (~11.8 dendrites), and at 20 μm for heterozygous KI (~8.4 dendrites) (**Fig. 5F**). When we compared AUC for d42 neurons, we identified a significant impairment in overall dendritic arborization in heterozygous and homozygous KI neurons compared to WT (WT: 1293 AU,

heterozygous KI: 822.5 AU, homozygous KI: 887.8 AU, $p<0.01$ for WT vs. heterozygous KI, $p<0.05$ for WT vs. homozygous KI) (**Fig. 5G**). Comparison of heterozygous and homozygous KI to ABE corrected neurons was trending but not significantly different (ABE corrected: 1174 AU, $p>0.05$). When we compared AUC between WT and ABE corrected neurons, we identified no differences in overall dendritic arborization ($p>0.05$), suggesting that ABE correction results in neurons with dendritic arborization phenotype in-between WT and KI variant neurons. We identified a similar impairment when we assessed total dendritic length in d42 neurons (**Fig. 5H**). Heterozygous and homozygous KI neurons had reduced total dendritic length compared to WT control neurons (WT: 1704.7 μm, heterozygous KI: 1086.4 μm, homozygous KI μm: 1093.8 μm, $p<0.05$). Once again, ABE corrected neurons were not significantly different from either WT or KI neurons (ABE corrected: 1536 μm, $p>0.05$). These findings support a developmental impairment arising from loss-of-function of wild-type neuroserpin activity in addition to the toxic gain-of-function of aggregating mutant neuroserpin.

eVLP-mediated delivery of ABEs can efficiently correct the FENIB variant.

Delivery of gene editors to target tissues is an outstanding challenge.[63,64] We decided to test eVLPs to target neurons due to the high efficiency of targeting and subsequent editing, and simple methods for reconfiguration. We aimed to produce eVLPs with VSV-G glycoprotein, MMLV-gag-pol, and MMLV fused NG-ABE8e ribonucleoprotein (**Fig. 6A**). We first tested eVLPs on target loci with established high editing; HEK2 and HEK3 (**Fig. 6B and C**).[34] To generate eVLPs, we transfected HEK293T cells with plasmids encoding the eVLP components and collected supernatant after 72 hours.[34] Next, we treated HEK293T cells with 100-fold concentrated eVLPs and sequenced the target loci 72 hours after treatment. We observed robust editing at both the HEK2 and HEK3 loci, with the greatest editing at the A7 position (87.98%±4.819, N=3) and A6 position (64.07%±1.652%, N=3), respectively.

After confirming the capacity of eVLPs to deliver ABE and edit target loci in the HEK293T cell line, we next sought to test eVLP editing in *SERPINI1* KI iPSCs. We treated homozygous KI iPSCs with eVLP containing supernatant in Stemflex iPSC media at ratios of 1:10, 1:3, and 1:1 (**Fig. S5A**). After 72 hours, we collected DNA from all cells treated with the eVLP and Sanger sequenced the samples at the *SERPINI1* c.1175 G>A locus. Without concentration or selection, we observed >10% editing at the A5 and A6 nucleotides in our 1:1 ratio of eVLP containing supernatant to Stemflex media. We next concentrated eVLPs as previously mentioned, and treated homozygous KI iPSCs and sequenced the target locus 72 hours after treatment without selection (**Fig. 6D**). eVLP editing using EditR revealed a dosage effect, with the 30 ul high dose editing resulting in 22.5% correction to the wild-type sequence at the A5 and 25% correction at the A6 positions.

We assessed neural editing by treating homozygous KI neurons with optimized eVLP conditions. Concentrated eVLPs were added with neurotrophic factors, ARAC, and doxycycline at d7 of neural induction. Treated neurons were collected without selection and Sanger sequenced at the target locus after 72 hours (**Fig. S5B**). We observed a dosage effect in our homozygous KI iNs. However, our highest dose, 30ul, only reached 2% at the A5 and 1.5% editing at the A6 position, necessitating further optimization.

We tested a modified rabies virus glycoprotein, FuG-B2, to increase eVLP uptake through enhancing neuronal specificity and selectivity.[34,65] Homozygous KI neurons treated with concentrated eVLPs enveloped with FuG-B2 glycoprotein increased editing to ~4% at the A5 and 2% at the A6 positions (**Fig. S5C**). To optimize neuron specific nuclear localization, we generated NG-ABE8e flanked by Nipah virus W protein (NiV W), methyl CpG binding protein 2 (MeCP2), and heterogenous nuclear ribonucleoprotein D (hnRNP D) NLSs (**Fig. 6A**).[37] We produced each NLS variant in eVLPs with both VSV-G and FuG-B2 glycoproteins. Homozygous KI neurons treated with NiV W NLS modified ABE demonstrated the highest correction at the A5 position

(1.7% VSV-G and 3.2% FuG-B2) but this was not statistically significant from BPSV40 (0.6% VSV-G, and 2.9% FuG-B2) (**Fig S5D and S5E**). MeCP2 and hnRNP D had significantly reduced editing at the A5 position with FuG-B2 glycoprotein (0.8% MeCP2 $p<0.05$, and 0.1% hnRNP D $p<0.001$). The difference in eVLP editing efficiencies between iPSCs and iPSC-derived neurons suggested an issue with eVLP uptake.

We hypothesized that eVLP-cell interactions were insufficient for efficient eVLP uptake and decided to test the addition of polybrene (**Fig. 6E**). Polybrene is a cationic polymer which facilitates receptor-independent virus adsorption.[66] Both 5 ug/ml and 10 ug/ml polybrene increased eVLP editing by 10-fold in VSV-G eVLPs. eVLP editing in homozygous KI neurons with VSV-G glycoprotein with 5 ug/ml polybrene had the highest editing efficiency at the A5 position (28%) while 10 ug/ml polybrene followed closely (18%).

We assessed eVLPs with neuron specific NLS with 5 ug/ml polybrene to determine optimal neuron editing. We treated homozygous KI neurons with VSV-G glycoprotein eVLPs and either BP/SV40 or neuron-specific NLS (**Fig. 6E**). VSV-G with NiV W NLS (38.5%, $p<0.0001$) had the highest editing efficiency, significantly greater than BP/SV40 (20.9%). We also found that MeCP2 NLS (29.7%, $p<0.01$) had statistically increased editing at the A5 position when compared to BP/SV40. hnRNP D (18.8% $p=0.76$) NLS did not statistically differ from BP/SV40. Neuron specific NLS eVLPs had different editing profiles than standard BP/SV40. There was low but detectable editing at all A positions along the gRNA. BP/SV40 had the broadest editing window with A5 (20.9%) A6 (13.7%). The neuronal NLS editors had a higher ratio of desired A5 to bystander A6 editing, with NiV W 38.5%:10.9%, MeCP2 29.7%:7.2%, and hnRNP D at 18.8%:4.7%. We assessed eVLP editing of MUT NS-GFP neurons (**Fig. S5F**). VSV-G with BP/SV40 NLS (13.4%) had the greatest editing efficiency at the A5 position. Unlike homozygous KI neurons, eVLP editing of the MUT NS-GFP loci by NiV W (4.8% $p<0.0001$), MeCP2 (0.4%, $p<0.0001$), and hnRNP D (0.16% $p<0.0001$) was statistically less efficient. Thus, neuron specific NLS eVLPs

increase editing efficiency in KI neurons and increased the desired A5 to bystander A6 editing ratio, but not in the MUT NS-GFP neurons.

Discussion

We aimed to generate patient-specific models of FENIB to assess whether ABEs can efficiently correct the pathogenic variant, and if preventing novel mutant protein expression would facilitate clearance of neuroserpin aggregates. Our results support that CRISPR/Cas genome editing systems can model and eliminate aggregates or prevent aggregation progression in this rare patient-specific variant of brain disease using HEK293T, iPSC, and neuron models.

We hypothesized that disease modifying treatments for FENIB would require resolving NS aggregation, similar to potential therapies for Alzheimer's and Huntington's diseases which target aggregate-prone protein precursors.[14,17] Doxycycline withdrawal experiments demonstrated that early prevention of mutant protein expression facilitates complete clearance of NS-GFP aggregates. Whether clearance of aggregates resulted from reduced aggregate burden or because neurons were younger remains unclear. The average number of aggregates per cell and size of aggregates were similar in day 10 neurons and day 21 neurons, suggesting that the difference in aggregate clearance reflected neuron age, not aggregate burden. In more mature neurons, we were unable to achieve complete clearance, but prevented further NS-GFP aggregation. Coupling prevention of novel protein with methods to promote protein turnover may facilitate aggregate clearance. Embelin, a small molecule derived from the Japanese Ardisia herb, prevented *in vitro* NS aggregation and dissolve aggregates.[67,68] ABE correction of the pathogenic variant to prevent new aggregation combined with embelin disruption of existing aggregates is a potential effective therapy.

Research of conformational neurodegenerative diseases is often limited by experimental timescale where aggregate burden requires aging over years or decades for accumulation and

neurotoxicity. [69,70] Overexpression of NS overcomes low levels and reduced overall duration of endogenous NS protein expression, and has been used to successfully study FENIB both in vitro and in vivo.[5,12,42,43,43,71–73] However, overexpression of NS-GFP to study aggregation obscures potential loss-of-function phenotypes which may arise given patients' heterozygosity. We complemented NS-GFP with heterozygous and homozygous KI neurons and identified a novel developmental deficit in dendritic arborization and total dendritic length. Dendritic spines are directly involved in receiving excitatory synaptic inputs in excitatory cortical neurons. Impaired dendritic spines are a known abnormality in epilepsy, but it remains unclear whether this is a cause or result of epilepsy.[74] Dendritic pathologies have been identified in neurological disorders with epilepsy including Rett and Down syndrome.[75,76] Approximately 90% of patients with Rett syndrome have epilepsy. Knockdown of endogenous *Mecp2*, the gene implicated in Rett syndrome, using shRNAs reduced the number of dendritic nodes, total dendritic length, and dendritic intersections in a neuronal model.[77] Further analysis into dendritic spines in FENIB will be illustrative to assess whether loss-of-function of NS in KI neurons results in impairments to spine morphology in addition to dendritic arbor.

Whole-cell patch clamp electrophysiology revealed no differences between WT and heterozygous or homozygous KI neurons, suggesting that a loss-of-function of normal NS protein does not directly cause seizures. Because our model generates cortical excitatory neurons, it remains possible that other neuronal subtypes, specifically inhibitory neurons, could be affected in FENIB. Additionally, our in vitro cultures may not sufficiently model the interactions between NS and tissue-type plasminogen activator (tPA). tPA, activates brain N-methyl-D-aspartate receptors (NMDAR) via direct cleavage of the NR1 subunit of NMDARs or a low-density lipoprotein receptor (LDLR) intermediate.[78,79] NS protects against NMDAR excitotoxicity *in vivo* and *in vitro* by limiting tPA's pro-excitotoxic effects.[80] Likely, further in vivo modelling of aged FENIB neurons will be

required to assess whether the NS-tPA and NMDAR interactions are responsible for the epileptic phenotype.

Delivery of genome editors larger than 5kb remains a challenge. eVLPs with neuron specific NLS improved editing efficiency of in vitro cortical excitatory neurons, and had the additional benefit of narrowing the on-target:bystander editing ratio. We envision that neuron-specific NLS's will improve editing with both AAV and lipid-nanoparticle RNPs, as both require NLSs for nuclear entry.

In summary, our CRISPR/Cas genome editors effectively modelled and corrected the severe FENIB variant. Our modelling strategy uses complementary cellular systems to investigate loss-of-function and toxic gain-of-function present in FENIB. Heterozygous and homozygous KI neurons revealed developmental deficits resulting in impaired dendritic morphology. Early termination of MUT NS-GFP expression can completely clear aggregates, while late termination prevented further NS-GFP aggregation. Treatment of MUT NS-GFP HEK293T with ABE facilitated NS-GFP clearance. Finally, we increased editing efficiency in neurons using NiV W NLS peptide to shuttle NG-ABE8e into neuronal nuclei.

Materials and Methods

iPSC culture

Induced pluripotent stem cells (iPSC) were cultured in Stemflex media (Gibco; Grand Island, NY) supplemented with 1% antibiotic-antimycotic (Gibco; Grand Island, NY) with daily media changes. Cells were split and passaged at 70% confluency, approximately every 3-4 days, using 0.5mM EDTA (Invitrogen; Waltham, MA) in DPBS (Gibco; Grand Island, NY) or Accutase (Innovative Cell Technologies; San Diego, CA) and plated onto geltrex (Gibco; Grand Island, NY) coated tissue culture treated wells. When passing, iPSCs were plated in Stemflex media with 1% antibiotic-antimycotic supplemented with 10uM ROCK-inhibitor (LC Laboratories; Woburn, MA). Cell media

was changed with Stemflex media without ROCK-inhibitor the following day. Cells were maintained at 37°C with 5.0% CO_2.

Neural induction

iPSC-derived neurons were generated through doxycycline (Sigma Aldrich; Saint Louis, MO) induced expression of Ngn2.[29] Briefly, iPSCs were detached and passaged onto geltrex coated plates, and transduced with lentivirus expressing ubiquitin-C promoter expressed reverse tetracycline transactivator, or tetracycline response element On promoter expressed mouse Neurogenin2-T2A-puromycin (*Ngn2*) resistance in Stemflex media with 10uM ROCK-inhibitor. On day 1, culturing media was changed to iN media consisting of Neurobasal medium (Gibco; Grand Island, NY) with 1X B-27 (Gibco; Grand Island, NY) and further supplemented with 10 uM ROCK-inhibitor and doxycycline to induce *Ngn2* expression. Culturing media was replaced every day with iN media until day 6, with doxycycline induction from days 1-7, and puromycin (Invivogen; San Diego, CA) selection from days 2-5. On day 6, cells were detached and replated onto glia isolated from p3 mouse pups in iN media supplemented with 5% FBS (GeminiBio; West Sacramento, CA) on either geltrex coated glass coverslips for IF and patch clamp electrophysiology or plastic tissue culture plates for RNA and protein processing. Beginning d7, culturing media was replaced every 2-3 days with iN media supplemented with BDNF (STEMCELL Technologies; Vancouver, Canada) GDNF (STEMCELL Technologies, Vancouver, Canada), NT-3 (STEMCELL Technologies; Vancouver, Canada), and ARAC (Selleckchem; Houston, TX). Cells were maintained at 37°C with 5.0% CO_2.

HEK 293T culture

HEK 293T cells were cultured in DMEM+/+ consisting of DMEM (Gibco; Grand Island, NY) supplemented with 10% fetal bovine serum (FBS) and 1% antibiotic antimycotic with media

changes every 2-3 days. Cells were passa Cells were maintained at 37°C with 5.0% CO_2. ged every 5-7 days or when 70% confluent using 0.25% trypsin/EDTA (Gibco; Grand Island, NY).

Plasmid generation

gRNAs targeting *SERPINI1* c.1175 G>A locus were cloned into pBSU6-FE-GFP plasmids. Plasmids were transformed into DH5A (Invitrogen; Waltham, MA) or Stbl3 (Invitrogen; Waltham, MA) bacteria, and amplified using Nucleobond xtra maxiprep plasmid purification kit (Macherey-Nagel; Allentown, PA). NG-ABEs, *SERPINI1* cDNA, and eVLPs with neuron specific NLS were generated using Gibson assembly.

Transfections

Transfections were performed using nucleofections, lipofectamine, or polyethylenimine. Nucleofections used 4D nucleofector system with P3 or SF reagent (Lonza; Morris Township, NJ) for iPSCs and HEK293T cells respectively, per manufacturer's guidelines. For generating the knock-in model, cells were nucleofected with 5 ug px458 or NG-px458 plasmid with locus specific gRNA and 5 ul of 10 uM ssODN (Integrated DNA technologies; Coralville, IA). Lipofection was performed using lipofectamine 2000 (Invitrogen; Waltham, MA) as reverse transfections, per manufacturer's guidelines. PEI (Sigma Aldrich; Saint Louis, MO) transfections were performed as reverse transfections, using a 1:5 ratio of plasmid to PEI in Opti-MEM (Gibco; Grand Island, NY).

Flow cytometry

HEK293T and iPS cells were dissociated into a single cell suspension and sorted 72-hours post-transfection using either a MoFlo-XDP or SY3200 cell sorter. For gene editing analysis, greater than 10,000 cells were collected and processed with DirectPCR lysis-reagent cell (Viagen; Los Angeles, CA) to extract crude DNA. GoTaq PCR (Promega; Madison, WI) was used to generate amplicon using sequence-specific primers (Integrated DNA technologies; Coralville, IA).. To

generate stable clones, cells were single cell sorted into 96-well plates into DMEM +/+ for HEK293Ts or Stemflex supplemented with CloneR (STEMCELL Technologies; Vancouver, Canada) for iPSCs.

T7E1 and Synthego ICE

T7 endonuclease I (T7E1) assay was performed by reannealing raw PCR product from GoTaq PCR amplification followed by incubation of reannealed product with T7E1 for digestion of mismatched paired strands. Synthego Ice analysis was performed by comparison of Sanger sequencing .ab1 files per application instructions.

Immunocytochemistry

Cells were plated on geltrex coated 12 mm No.1 coverslips (Chemglass Life Sciences; Vineland, NJ) in a 24-well plate. At experimental endpoints, cells were washed with DPBS to remove residual media, then fixed in 4% PFA (Electron Microscopy Sciences; Hatfield, PA) in PBS at room temperature. Samples were subsequently permeabilized using 0.1% triton-x 100 (Sigma Aldrich; Saint Louis, MO) in PBS, washed three times with PBS, then blocked using 10% donkey serum (Abcam; Waltham, MA), 0.25% triton-x 100 in PBS, and washed three times with PBS. Cells were incubated with primary antibodies overnight at 4C. The following day, cells were washed three times with PBS and incubated with secondary antibodies in 10% donkey serum in PBS for 1 hour at room temperature. Nuclei were stained with DAPI (Invitrogen; Waltham, MA), then stained slides were mounted with fluorescence mounting medium (Dako; Glostrup, Denmark). Cells were imaged with a Zeiss-880 inverted confocal microscope with a magnification of 40X N.A. 1.1, 1 Airy unit pinhole, half-maximal optimized Z-stack increments with 2x2 tiled images.

Western Blot

Cells were lysed using a lysis buffer containing 20 mM Tris-HCl, pH 7.5, 150 mM NaCl, cOmplete mini EDTA-free protease inhibitor cocktail (Roche; Indianapolis, IN), PhosSTOP phosphatase inhibitor cocktail (Roche; Indianapolis, IN), 1% Triton-X 100, in PBS. Samples were incubated on ice for 30 minutes and vortexed every 10 minutes. Samples were centrifuged at 20,000 RCF for 30 minutes at 4C to remove insoluble material.

Protein concentration was determined using the Pierce BCA kit (Thermo Fisher Scientific; Waltham, MA). 25 ug of whole cell lysate was loaded into a 7.5% mini-protein precast protein gel (Bio-Rad; Hercules, CA). Lysate for SDS-PAGE was prepared in 4X sample buffer with 2-mercaptoethanol (Sigma Aldrich; Saint Louis, MO) and heated at 98C for 5 minutes. Lysate for native-PAGE was prepared with BlueJuice Gel loading buffer (Thermo Fisher Scientific; Waltham, MA). Gels were run at 180V for 1 hour at 4C in either SDS-PAGE (25 mM Tris, 192 mM glycine, 1% SDS in diH2O) or native-PAGE running buffer (25 mM Tris, 192 mM glycine in diH2O) to separate proteins. Gels were electrophoretically transferred onto immun-blot PVDF membrane (Bio-Rad; Hercules, CA) overnight in transfer buffer (25 mM Tris, 190 mM glycine, 0.1% SDS, 20% methanol in diH2O) at a constant 20mA. Membranes were washed with TBST (20 mM Tris, 150 mM NaCl, 0.1% tween 20 in diH2O) then blocked in 5% nonfat dry milk in TBST. Membranes were rotationally incubated with diluted primary antibodies in 5% nonfat dry milk in TBST at 4C overnight. The following day, membranes were washed with TBST and incubated for 1 hour at room temperature with HRP-conjugated secondary antibody (Invitrogen; Waltham, MA) in TBST. Membranes were washed three times with TBST, and a final wash with TBS before applying Western Blotting Luminol Reagent (Santa Cruz Biotechnology; Dallas, TX) and imaging with a Bio Rad ChemiDoc imaging system.

RNA extraction and cDNA synthesis

RNA was extracted using RNeasy mini kit (Qiagen; Hilden, Germany) with on-column DNase digestion (Qiagen; Hilden, Germany) per the manufacturer's guidelines. cDNA was synthesized

from RNA using the SuperScript III First-Strand cDNA Synthesis Kit (Thermo Fisher Scientific; Waltham, MA).

Quantitative PCR

Quantitative PCR was performed on cDNA synthesized as mentioned above using ssoAdvanced Universal SYBR Green Supermix reagent (Bio-Rad; Hercules, CA). For each assay, 500 nM of forward and reverse primers, and 1X final concentration of SYBR green master mix was used. Assays were performed using a StepOne Real-time PCR system (Applied Biosystems; Waltham,MA) using the following settings: 30 seconds at 95°C, followed by 40 cycles of 10 seconds at 95°C and 60 seconds at 60°C, followed by a melt curve analysis of 40 cycles at 65°C -95°C increasing in 0.5°C increments at a rate of 5 seconds per step.

Next generation sequencing

RNA was extracted using RNeasy mini kit as mentioned above. Automated polyA selected stranded RNA-seq library prep was performed by the New York University Langone Health Genome Technology Center. Libraries were sequenced using an Illumina NovaSeq6000 next generation sequencer (Illumina Inc; San Diego, CA) as paired end runs. After quality control, samples were mapped using BBTools software, Sequence Expression Analyzer (Seal) (Joint Genome Institute; Berkeley, CA) against both mouse and human reference genomes to exclude reads from mouse glia.[81] Reads were mapped using Spliced Transcripts Aligned to a Reference (STAR), and counted with featureCounts.[82,83] Read counts were normalized as transcripts per million (TPM) and plotted as $\log_2(TPM+1)$.

Aggregate analysis

Aggregate analysis was performed using ImageJ FIJI software. Briefly, images were acquired using a Zeiss-880 inverted confocal microscope at 40X magnification. Images were projected as maximum projections of Z-stack images to create a two-dimensional image of aggregates. The

NS-GFP channel was separated and thresholded for the brightest fluorescence expression. All images from one experiment were thresholded the same. Aggregates were counted using ImageJ "analyze particles" function. Particles of less than 0.1 microns were excluded to avoid including single pixel values in the analysis.

Cell count

Cells from confocal images were identified and counted using Cellpose v2.2.2 software.[84] Briefly, images were initially processed in ImageJ to isolate DAPI stained nuclei channels. Nuclei channels were opened in cellpose set to nuclei mode. Cell diameter was automatically determined using the calibration function. Flow_threshold was set to 0.4, cellprob_threshold was set to 0.0, and stitch_threshold was set to 0.0. Image saturation was set to automatic.

Sholl analysis

iPSC-derived neurons were cultured in geltrex coated 12 mm No.1 coverslips. Neurons were transfected with pmaxGFP™ (Lonza; Morris Township, NJ) using Lipofectamine 2000 to sparsely label neurons. 24-hours post-transfection, cells were fixed with 4% PFA in PBS. Cells were stained with GFP Recombinant Rabbit Monoclonal Antibody (Invitrogen; Waltham, MA) at 1:100 dilution, incubated at 4C overnight and then labeled with Donkey anti-Rabbit IgG (H+L) Cross-Adsorbed Secondary Antibody, DyLight™ 488 (Invitrogen; Waltham, MA) at 1:250 dilution. Coverslips were mounted on slides using Dako fluorescent mounting media.

Neurite morphology analyses on transfected iPSC-derived neurons were performed on randomly sampled neurons. Images of neurons were acquired using the Zeiss-880 confocal at 63X magnification with 1 Airy unit pinhole, Z-stack increments of 4.28 µm, and laser gain between 700-800 for all channels. Imaging parameters were kept consistent between inductions. Images were processed using NIH image software (ImageJ) as a maximum projection of 2x2 tiled images. Neurites were manually traced using NIH ImageJ with the SNT plugin and Sholl analysis was

performed using Image J with the Sholl analysis plugin. To ensure accuracy, neurons with overlapping neurites were excluded from analysis.

Electrophysiology

Whole-cell patch clamp recording was performed on iPSC-derived neurons 42-44 days after neural induction. Glass pipettes were filled with a solution containing the following (in mM): 135 $KmeSO_3$, 5 KCl, 0.1 EGTA, 10 HEPES, 2 NaCl, 5 MgATP, 0.4 Na_2GTP, 10 $Na_2PhosphoCreatine$ (pH 7.3). Cells were perfused with artificial cerebrospinal fluid (ACSF) containing (in mM)- 125 NaCl, 22.5 D-glucose, 25 $NaHCO_3$, 2.5 KCl, 1.25 NaH_2PO_4, 3 $C_3H_3NaO_3$, 1 $C_6H_8O_6$, 2 CaCl, 1 MgCl, saturated with 95% O_2, 5% CO_2 (pH 7.3). The ACSF was continuously flowing at a rate of 2-3 mL/min at room temperature. Recording electrodes were pulled from borosilicate glass pipettes (Sutter Instrument; Novato, CA) and had a tip resistance of 3 – 5 MΩ when filled with internal solution. All recordings were performed using a MultiClamp 700B amplifier interfaced with a PC through a Digidata 1550 (Molecular Devices; Sunnyvale, CA). Data was acquired with pClamp 10.7 software (Molecular Devices; Sunnyvale, CA) and analyzed with Clampfit 10.7 (Molecular Devices; Sunnyvale, CA) and Prism (Graphpad; LaJolla; CA).

ABE-eVLP production and purification

ABE-eVLPs were generated by transfection using PEI. 1.2 x 10^7 HEK 293T cells were reverse transfected with VSV-G (400 ng), MMLVgag-pro-pol (3,375 ng), MMLVgag-3XNES-NG-ABE8e (1,125 ng), and sgRNA (4,400 ng) plasmids per 10 cm dish. 72-hours post-transfection, eVLP containing media was harvested and centrifuged for 10 min at 500 RCF to pellet cells. eVLP containing supernatant was filtered using a 0.45 um PVDF syringe filter (Corning; Corning, NY). eVLP supernatant was concentrated 100-fold using Lenti-X concentrator (Takara Bio; Shiga, Japan) or PEG-IT virus precipitation solution (System Biosciences; Palo Alto, CA) per manufacturer's instructions in cold 1 X DPBS. Concentrated eVLP was either immediately used or stored at -80C avoiding multiple freeze-thaws.

eVLP delivery of ABE

eVLP delivery of ABE was performed by adding concentrated eVLP to HEK293T, iPSC, or glia cocultured iNs. For iPSCs, cells were gently dissociated into a single cell suspension with Accutase treatment and 40,000 cells were plated on geltrex coated 48-well plates. Concentrated eVLP was treated as a reverse transduction and media was changed at 24 hours. All cells were collected for analysis without selection at 72 hours. For iNs, cells were plated as normal onto glia coated cultureware. Concentrated eVLP was added at the indicated timepoint as part of a standard media change with the addition of 10ug/ml polybrene (Sigma Aldrich; Saint Louis, MO). Media was changed the following day with complete iN media with neurotrophic factors. Cells were collected for analysis without selection at 72 hours.

Statistics

All statistical analyses were computed using Prism as described. Graphs are presented as means ± standard error of the mean (SEM), or box and whisker plots showing 10-90th percentile range, with sample number indicated per experiment. Unpaired Student's t tests, and one-way ANOVA with multiple comparisons tests were performed to determine p values with statistical significance at 95% confidence interval.

Data availability statement

For original data, please contact corresponding authors chengzu.long@nyumc.org, Jayeeta.Basu@nyulangone.org, and od4@nyu.edu.

Acknowledgements

We would like to acknowledge members of the Long and Basu labs for comments and technical assistance. We would like to thank members of the NYU Langone core facilities including Cytometry and Cell Sorting Laboratory, Genome Technology Center, High Performance

Computing Core, Small Instrument Fleet, and Microscopy Laboratory for their technical assistance. This work was supported by grants from the Departmental Start-Up Grant, NYU Langone Health, Kids Connect Charitable Fund, NIH (T32GM136542), NYU Clinical and Translational Science Institute (CTSI) Pilot Project (UL1TR001445, NIH/NCATS (JB/CL/OD/TB)), and Cancer Center Support Grant (P30CA016086).

Author contributions

C.T.K. and C.L. conceptualized the project. C.T.K., T.B., O.D., J.B., and C.L. acquired funding. C.T.K. and N.M. performed experiments and analyzed results. T.B. and Q.Y. offered training, guidance, and oversaw experiments. V.Z., D.K., M.P. provided technical support. C.T.K. and C.L. wrote the manuscript. C.T.K., N.M., T.B., O.D., J.B., and C.L. reviewed and edited the manuscript.

Declaration of interests

The authors declare no competing interests.

Keywords

Protein conformational disease

Protein aggregation

iPSC-derived neurons

CRISPR/Cas9

Adenine base editing

Engineered virus-like particles

References

1. Chiti, F., and Dobson, C.M. (2006). Protein Misfolding, Functional Amyloid, and Human Disease. Annual Review of Biochemistry *75*, 333–366. 10.1146/annurev.biochem.75.101304.123901.

2. Soto, C., and Pritzkow, S. (2018). Protein misfolding, aggregation, and conformational strains in neurodegenerative diseases. Nat Neurosci *21*, 1332–1340. 10.1038/s41593-018-0235-9.

3. Stoeckli, E.T., Lemkin, P.F., Kuhn, T.B., Ruegg, M.A., Heller, M., and Sonderegger, P. (1989). Identification of proteins secreted from axons of embryonic dorsal-root-ganglia neurons. European Journal of Biochemistry *180*, 249–258. 10.1111/j.1432-1033.1989.tb14640.x.

4. Osterwalder, T., Contartese, J., Stoeckli, E.T., Kuhn, T.B., and Sonderegger, P. (1996). Neuroserpin, an axonally secreted serine protease inhibitor. The EMBO Journal *15*, 2944–2953. 10.1002/j.1460-2075.1996.tb00657.x.

5. Miranda, E., Römisch, K., and Lomas, D.A. (2004). Mutants of Neuroserpin That Cause Dementia Accumulate as Polymers within the Endoplasmic Reticulum*. Journal of Biological Chemistry *279*, 28283–28291. 10.1074/jbc.M313166200.

6. Belorgey, D., Crowther, D.C., Mahadeva, R., and Lomas, D.A. (2002). Mutant Neuroserpin (S49P) That Causes Familial Encephalopathy with Neuroserpin Inclusion Bodies Is a Poor Proteinase Inhibitor and Readily Forms Polymers in Vitro *. Journal of Biological Chemistry *277*, 17367–17373. 10.1074/jbc.M200680200.

7. López-González, I., Pérez-Mediavilla, A., Zamarbide, M., Carmona, M., Torrejón Escribano, B., Glatzel, M., Galliciotti, G., and Ferrer, I. (2016). Limited Unfolded Protein Response and Inflammation in Neuroserpinopathy. J Neuropathol Exp Neurol *75*, 121–133. 10.1093/jnen/nlv011.

8. Davis, R.L., Holohan, P.D., Shrimpton, A.E., Tatum, A.H., Daucher, J., Collins, G.H., Todd, R., Bradshaw, C., Kent, P., Feiglin, D., et al. (1999). Familial Encephalopathy with Neuroserpin Inclusion Bodies. The American Journal of Pathology *155*, 1901–1913. 10.1016/S0002-9440(10)65510-1.

9. Davis, R.L., Shrimpton, A.E., Carrell, R.W., Lomas, D.A., Gerhard, L., Baumann, B., Lawrence, D.A., Yepes, M., Kim, T.S., Ghetti, B., et al. (2002). Association between conformational mutations in neuroserpin and onset and severity of dementia. The Lancet *359*, 2242–2247. 10.1016/S0140-6736(02)09293-0.

10. Kara, B., Sarıkaya, C.E., Bayrak, Y.E., Güneş, A.S., Güngör, M., and Yeşil, G. (2020). Early-onset rapidly progressive myoclonic epilepsy associated with G392R likely pathogenic variant in SERPINI1. Seizure *80*, 181–182. 10.1016/j.seizure.2020.06.022.

11. Knupp, K., and Wirrell, E. (2014). Progressive myoclonic epilepsies: It takes a village to make a diagnosis. Neurology *82*, 378–379. 10.1212/WNL.0000000000000091.

12. Guadagno, N.A., Moriconi, C., Licursi, V., D'Acunto, E., Nisi, P.S., Carucci, N., De Jaco, A., Cacci, E., Negri, R., Lupo, G., et al. (2017). Neuroserpin polymers cause oxidative stress in a neuronal model of the dementia FENIB. Neurobiology of Disease *103*, 32–44. 10.1016/j.nbd.2017.03.010.

13. Levey, A.I. (2021). Progress with Treatments for Alzheimer's Disease. New England Journal of Medicine *384*, 1762–1763. 10.1056/NEJMe2103722.

14. Tabrizi, S.J., Flower, M.D., Ross, C.A., and Wild, E.J. (2020). Huntington disease: new insights into molecular pathogenesis and therapeutic opportunities. Nat Rev Neurol *16*, 529–546. 10.1038/s41582-020-0389-4.

15. Evers, M.M., Miniarikova, J., Juhas, S., Vallès, A., Bohuslavova, B., Juhasova, J., Skalnikova, H.K., Vodicka, P., Valekova, I., Brouwers, C., et al. (2018). AAV5-miHTT Gene Therapy Demonstrates Broad Distribution and Strong Human Mutant Huntingtin Lowering in a Huntington's Disease Minipig Model. Molecular Therapy *26*, 2163–2177. 10.1016/j.ymthe.2018.06.021.

16. Tabrizi, S.J., Leavitt, B.R., Landwehrmeyer, G.B., Wild, E.J., Saft, C., Barker, R.A., Blair, N.F., Craufurd, D., Priller, J., Rickards, H., et al. (2019). Targeting Huntingtin Expression in Patients with Huntington's Disease. N Engl J Med *380*, 2307–2316. 10.1056/NEJMoa1900907.

17. Cummings, J., Zhou, Y., Lee, G., Zhong, K., Fonseca, J., and Cheng, F. (2023). Alzheimer's disease drug development pipeline: 2023. Alzheimer's & Dementia: Translational Research & Clinical Interventions *9*, e12385. 10.1002/trc2.12385.

18. Wild, E.J., and Tabrizi, S.J. (2017). Therapies targeting DNA and RNA in Huntington's disease. The Lancet Neurology *16*, 837–847. 10.1016/S1474-4422(17)30280-6.

19. Mali, P., Yang, L., Esvelt, K.M., Aach, J., Guell, M., DiCarlo, J.E., Norville, J.E., and Church, G.M. (2013). RNA-Guided Human Genome Engineering via Cas9. Science *339*, 823–826. 10.1126/science.1232033.

20. Cong, L., Ran, F.A., Cox, D., Lin, S., Barretto, R., Habib, N., Hsu, P.D., Wu, X., Jiang, W., Marraffini, L.A., et al. (2013). Multiplex Genome Engineering Using CRISPR/Cas Systems. Science *339*, 819–823. 10.1126/science.1231143.

21. Jinek, M., Chylinski, K., Fonfara, I., Hauer, M., Doudna, J.A., and Charpentier, E. (2012). A Programmable Dual-RNA–Guided DNA Endonuclease in Adaptive Bacterial Immunity. Science *337*, 816–821. 10.1126/science.1225829.

22. Chapman, J.R., Taylor, M.R.G., and Boulton, S.J. (2012). Playing the End Game: DNA Double-Strand Break Repair Pathway Choice. Molecular Cell *47*, 497–510. 10.1016/j.molcel.2012.07.029.

23. Urnov, F.D., Rebar, E.J., Holmes, M.C., Zhang, H.S., and Gregory, P.D. (2010). Genome editing with engineered zinc finger nucleases. Nat Rev Genet *11*, 636–646. 10.1038/nrg2842.

24. Long, C., Amoasii, L., Mireault, A.A., McAnally, J.R., Li, H., Sanchez-Ortiz, E., Bhattacharyya, S., Shelton, J.M., Bassel-Duby, R., and Olson, E.N. (2016). Postnatal genome editing partially restores dystrophin expression in a mouse model of muscular dystrophy. Science *351*, 400–403. 10.1126/science.aad5725.

25. Park, H., Oh, J., Shim, G., Cho, B., Chang, Y., Kim, S., Baek, S., Kim, H., Shin, J., Choi, H., et al. (2019). In vivo neuronal gene editing via CRISPR–Cas9 amphiphilic nanocomplexes alleviates deficits in mouse models of Alzheimer's disease. Nat Neurosci *22*, 524–528. 10.1038/s41593-019-0352-0.

26. Yin, H., Xue, W., Chen, S., Bogorad, R.L., Benedetti, E., Grompe, M., Koteliansky, V., Sharp, P.A., Jacks, T., and Anderson, D.G. (2014). Genome editing with Cas9 in adult mice corrects a disease mutation and phenotype. Nat Biotechnol *32*, 551–553. 10.1038/nbt.2884.

27. Chang, C.-J., Kotini, A., Teruya-Feldstein, J., Abdel-Wahab, O., Bradley, R., and Papapetrou, E.P. (2016). Isogenic iPSC Models of SRSF2-Mutant Myelodysplastic Syndrome Capture Disease Phenotypes, Splicing Defects and Drug Responses. Blood *128*, 962–962. 10.1182/blood.V128.22.962.962.

28. Xie, Y., Ng, N.N., Safrina, O.S., Ramos, C.M., Ess, K.C., Schwartz, P.H., Smith, M.A., and O'Dowd, D.K. (2020). Comparisons of dual isogenic human iPSC pairs identify functional alterations directly caused by an epilepsy associated SCN1A mutation. Neurobiology of Disease *134*, 104627. 10.1016/j.nbd.2019.104627.

29. Zhang, Y., Pak, C., Han, Y., Ahlenius, H., Zhang, Z., Chanda, S., Marro, S., Patzke, C., Acuna, C., Covy, J., et al. (2013). Rapid Single-Step Induction of Functional Neurons from Human Pluripotent Stem Cells. Neuron *78*, 785–798. 10.1016/j.neuron.2013.05.029.

30. Vítor, A.C., Huertas, P., Legube, G., and de Almeida, S.F. (2020). Studying DNA Double-Strand Break Repair: An Ever-Growing Toolbox. Frontiers in Molecular Biosciences *7*.

31. Mao, Z., Bozzella, M., Seluanov, A., and Gorbunova, V. (2008). DNA repair by nonhomologous end joining and homologous recombination during cell cycle in human cells. Cell Cycle *7*, 2902–2906. 10.4161/cc.7.18.6679.

32. Saleh-Gohari, N., and Helleday, T. (2004). Conservative homologous recombination preferentially repairs DNA double-strand breaks in the S phase of the cell cycle in human cells. Nucleic Acids Research *32*, 3683–3688. 10.1093/nar/gkh703.

33. Gaudelli, N.M., Komor, A.C., Rees, H.A., Packer, M.S., Badran, A.H., Bryson, D.I., and Liu, D.R. (2017). Programmable base editing of A•T to G•C in genomic DNA without DNA cleavage. Nature *551*, 464–471. 10.1038/nature24644.

34. Banskota, S., Raguram, A., Suh, S., Du, S.W., Davis, J.R., Choi, E.H., Wang, X., Nielsen, S.C., Newby, G.A., Randolph, P.B., et al. (2022). Engineered virus-like particles for efficient in vivo delivery of therapeutic proteins. Cell *185*, 250-265.e16. 10.1016/j.cell.2021.12.021.

35. Choi, J.G., Dang, Y., Abraham, S., Ma, H., Zhang, J., Guo, H., Cai, Y., Mikkelsen, J.G., Wu, H., Shankar, P., et al. (2016). Lentivirus pre-packed with Cas9 protein for safer gene editing. Gene Ther *23*, 627–633. 10.1038/gt.2016.27.

36. Lyu, P., Wang, L., and Lu, B. (2020). Virus-Like Particle Mediated CRISPR/Cas9 Delivery for Efficient and Safe Genome Editing. Life (Basel) *10*, 366. 10.3390/life10120366.

37. Karasev, M.M., Baloban, M., Verkhusha, V.V., and Shcherbakova, D.M. (2022). Nuclear Localization Signals for Optimization of Genetically Encoded Tools in Neurons. Frontiers in Cell and Developmental Biology *10*.

38. Nishimasu, H., Shi, X., Ishiguro, S., Gao, L., Hirano, S., Okazaki, S., Noda, T., Abudayyeh, O.O., Gootenberg, J.S., Mori, H., et al. (2018). Engineered CRISPR-Cas9 nuclease with expanded targeting space. Science *361*, 1259–1262. 10.1126/science.aas9129.

39. Richardson, C.D., Ray, G.J., DeWitt, M.A., Curie, G.L., and Corn, J.E. (2016). Enhancing homology-directed genome editing by catalytically active and inactive CRISPR-Cas9 using asymmetric donor DNA. Nature Biotechnology *34*, 339–344. 10.1038/nbt.3481.

40. Synthego Performance Analysis, ICE analysis. 2019. v3.0. Sythego.

41. Fra, A., D'Acunto, E., Laffranchi, M., and Miranda, E. (2018). Cellular Models for the Serpinopathies. In Serpins: Methods and Protocols Methods in Molecular Biology., A. Lucas, ed. (Springer), pp. 109–121. 10.1007/978-1-4939-8645-3_7.

42. D'Acunto, E., Gianfrancesco, L., Serangeli, I., D'Orsi, M., Sabato, V., Guadagno, N.A., Bhosale, G., Caristi, S., Failla, A.V., De Jaco, A., et al. (2022). Polymerogenic neuroserpin causes mitochondrial alterations and activates NFκB but not the UPR in a neuronal model of neurodegeneration FENIB. Cell. Mol. Life Sci. *79*, 437. 10.1007/s00018-022-04463-3.

43. Miranda, E., MacLeod, I., Davies, M.J., Pérez, J., Römisch, K., Crowther, D.C., and Lomas, D.A. (2008). The intracellular accumulation of polymeric neuroserpin explains the severity of the dementia FENIB. Human Molecular Genetics *17*, 1527–1539. 10.1093/hmg/ddn041.

44. Lindhout, F.W., Kooistra, R., Portegies, S., Herstel, L.J., Stucchi, R., Snoek, B.L., Altelaar, A.M., MacGillavry, H.D., Wierenga, C.J., and Hoogenraad, C.C. (2020). Quantitative mapping of transcriptome and proteome dynamics during polarization of human iPSC-derived neurons. eLife *9*, e58124. 10.7554/eLife.58124.

45. Gunhanlar, N., Shpak, G., van der Kroeg, M., Gouty-Colomer, L.A., Munshi, S.T., Lendemeijer, B., Ghazvini, M., Dupont, C., Hoogendijk, W.J.G., Gribnau, J., et al. (2018). A simplified protocol for differentiation of electrophysiologically mature neuronal networks from human induced pluripotent stem cells. Mol Psychiatry *23*, 1336–1344. 10.1038/mp.2017.56.

46. Espuny-Camacho, I., Michelsen, K.A., Gall, D., Linaro, D., Hasche, A., Bonnefont, J., Bali, C., Orduz, D., Bilheu, A., Herpoel, A., et al. (2013). Pyramidal Neurons Derived from Human Pluripotent Stem Cells Integrate Efficiently into Mouse Brain Circuits In Vivo. Neuron *77*, 440–456. 10.1016/j.neuron.2012.12.011.

47. Simkin, D., Marshall, K.A., Vanoye, C.G., Desai, R.R., Bustos, B.I., Piyevsky, B.N., Ortega, J.A., Forrest, M., Robertson, G.L., Penzes, P., et al. (2021). Dyshomeostatic modulation of Ca2+-activated K+ channels in a human neuronal model of KCNQ2 encephalopathy. eLife *10*, e64434. 10.7554/eLife.64434.

48. Budrikis, Z., Costantini, G., La Porta, C.A.M., and Zapperi, S. (2014). Protein accumulation in the endoplasmic reticulum as a non-equilibrium phase transition. Nat Commun *5*, 3620. 10.1038/ncomms4620.

49. Kopach, O., Esteras, N., Wray, S., Abramov, A.Y., and Rusakov, D.A. (2021). Genetically engineered MAPT 10+16 mutation causes pathophysiological excitability of human iPSC-derived neurons related to 4R tau-induced dementia. Cell Death Dis *12*, 1–12. 10.1038/s41419-021-04007-w.

50. Virdi, G.S., Choi, M.L., Evans, J.R., Yao, Z., Athauda, D., Strohbuecker, S., Nirujogi, R.S., Wernick, A.I., Pelegrina-Hidalgo, N., Leighton, C., et al. (2022). Protein aggregation and calcium dysregulation are hallmarks of familial Parkinson's disease in midbrain dopaminergic neurons. npj Parkinsons Dis. *8*, 1–22. 10.1038/s41531-022-00423-7.

51. Gehrke, J.M., Cervantes, O., Clement, M.K., Wu, Y., Zeng, J., Bauer, D.E., Pinello, L., and Joung, J.K. (2018). An APOBEC3A-Cas9 base editor with minimized bystander and off-target activities. Nature Biotechnology *36*, 977–982. 10.1038/nbt.4199.

52. Grünewald, J., Zhou, R., Iyer, S., Lareau, C.A., Garcia, S.P., Aryee, M.J., and Joung, J.K. (2019). CRISPR DNA base editors with reduced RNA off-target and self-editing activities. Nature Biotechnology *37*, 1041–1048. 10.1038/s41587-019-0236-6.

53. Rees, H.A., Wilson, C., Doman, J.L., and Liu, D.R. (2019). Analysis and minimization of cellular RNA editing by DNA adenine base editors. Science Advances *5*, eaax5717. 10.1126/sciadv.aax5717.

54. Koblan, L.W., Doman, J.L., Wilson, C., Levy, J.M., Tay, T., Newby, G.A., Maianti, J.P., Raguram, A., and Liu, D.R. (2018). Improving cytidine and adenine base editors by expression optimization and ancestral reconstruction. Nature Biotechnology *36*, 843–846. 10.1038/nbt.4172.

55. Richter, M.F., Zhao, K.T., Eton, E., Lapinaite, A., Newby, G.A., Thuronyi, B.W., Wilson, C., Koblan, L.W., Zeng, J., Bauer, D.E., et al. (2020). Phage-assisted evolution of an adenine base editor with improved Cas domain compatibility and activity. Nature Biotechnology *38*, 883–891. 10.1038/s41587-020-0453-z.

56. Kluesner, M.G., Nedveck, D.A., Lahr, W.S., Garbe, J.R., Abrahante, J.E., Webber, B.R., and Moriarity, B.S. (2018). EditR: A Method to Quantify Base Editing from Sanger Sequencing. CRISPR J *1*, 239–250. 10.1089/crispr.2018.0014.

57. Hermann, M., Reumann, R., Schostak, K., Kement, D., Gelderblom, M., Bernreuther, C., Frischknecht, R., Schipanski, A., Marik, S., Krasemann, S., et al. (2020). Deficits in developmental neurogenesis and dendritic spine maturation in mice lacking the serine protease inhibitor neuroserpin. Molecular and Cellular Neuroscience *102*, 103420. 10.1016/j.mcn.2019.103420.

58. Borges, V.M., Lee, T.W., Christie, D.L., and Birch, N.P. (2010). Neuroserpin regulates the density of dendritic protrusions and dendritic spine shape in cultured hippocampal neurons. Journal of Neuroscience Research *88*, 2610–2617. 10.1002/jnr.22428.

59. Kement, D., Reumann, R., Schostak, K., Voß, H., Douceau, S., Dottermusch, M., Schweizer, M., Schlüter, H., Vivien, D., Glatzel, M., et al. (2021). Neuroserpin Is Strongly Expressed in the Developing and Adult Mouse Neocortex but Its Absence Does Not Perturb Cortical Lamination and Synaptic Proteome. Front Neuroanat *15*, 627896. 10.3389/fnana.2021.627896.

60. Reumann, R., Vierk, R., Zhou, L., Gries, F., Kraus, V., Mienert, J., Romswinkel, E., Morellini, F., Ferrer, I., Nicolini, C., et al. (2017). The serine protease inhibitor neuroserpin is required for normal synaptic plasticity and regulates learning and social behavior. Learn. Mem. *24*, 650–659. 10.1101/lm.045864.117.

61. Arshadi, C., Günther, U., Eddison, M., Harrington, K.I.S., and Ferreira, T.A. (2021). SNT: a unifying toolbox for quantification of neuronal anatomy. Nat Methods *18*, 374–377. 10.1038/s41592-021-01105-7.

62. Ferreira, T.A., Blackman, A.V., Oyrer, J., Jayabal, S., Chung, A.J., Watt, A.J., Sjöström, P.J., and van Meyel, D.J. (2014). Neuronal morphometry directly from bitmap images. Nat Methods *11*, 982–984. 10.1038/nmeth.3125.

63. Raguram, A., Banskota, S., and Liu, D.R. (2022). Therapeutic in vivo delivery of gene editing agents. Cell *185*, 2806–2827. 10.1016/j.cell.2022.03.045.

64. Wang, D., Zhang, F., and Gao, G. (2020). CRISPR-Based Therapeutic Genome Editing: Strategies and In Vivo Delivery by AAV Vectors. Cell *181*, 136–150. 10.1016/j.cell.2020.03.023.

65. Kato, S., Kobayashi, K., Inoue, K., Kuramochi, M., Okada, T., Yaginuma, H., Morimoto, K., Shimada, T., Takada, M., and Kobayashi, K. (2011). A Lentiviral Strategy for Highly Efficient Retrograde Gene Transfer by Pseudotyping with Fusion Envelope Glycoprotein. Human Gene Therapy *22*, 197–206. 10.1089/hum.2009.179.

66. Davis, H.E., Morgan, J.R., and Yarmush, M.L. (2002). Polybrene increases retrovirus gene transfer efficiency by enhancing receptor-independent virus adsorption on target cell membranes. Biophysical Chemistry *97*, 159–172. 10.1016/S0301-4622(02)00057-1.

67. Visentin, C., Musso, L., Broggini, L., Bonato, F., Russo, R., Moriconi, C., Bolognesi, M., Miranda, E., Dallavalle, S., Passarella, D., et al. (2020). Embelin as Lead Compound for New Neuroserpin Polymerization Inhibitors. Life *10*, 111. 10.3390/life10070111.

68. Saga, G., Sessa, F., Barbiroli, A., Santambrogio, C., Russo, R., Sala, M., Raccosta, S., Martorana, V., Caccia, S., Noto, R., et al. (2016). Embelin binds to human neuroserpin and impairs its polymerisation. Sci Rep *6*, 18769. 10.1038/srep18769.

69. Penney, J., Ralvenius, W.T., and Tsai, L.-H. (2020). Modeling Alzheimer's disease with iPSC-derived brain cells. Mol Psychiatry *25*, 148–167. 10.1038/s41380-019-0468-3.

70. LaFerla, F.M., and Green, K.N. (2012). Animal Models of Alzheimer Disease. Cold Spring Harb Perspect Med *2*, a006320. 10.1101/cshperspect.a006320.

71. Kroeger, H., Miranda, E., MacLeod, I., Pérez, J., Crowther, D.C., Marciniak, S.J., and Lomas, D.A. (2009). Endoplasmic Reticulum-associated Degradation (ERAD) and

Autophagy Cooperate to Degrade Polymerogenic Mutant Serpins. J. Biol. Chem. *284*, 22793–22802. 10.1074/jbc.M109.027102.

72. Davies, M.J., Miranda, E., Roussel, B.D., Kaufman, R.J., Marciniak, S.J., and Lomas, D.A. (2009). Neuroserpin Polymers Activate NF-κB by a Calcium Signaling Pathway That Is Independent of the Unfolded Protein Response. J. Biol. Chem. *284*, 18202–18209. 10.1074/jbc.M109.010744.

73. Roussel, B.D., Newton, T.M., Malzer, E., Simecek, N., Haq, I., Thomas, S.E., Burr, M.L., Lehner, P.J., Crowther, D.C., Marciniak, S.J., et al. (2013). Sterol metabolism regulates neuroserpin polymer degradation in the absence of the unfolded protein response in the dementia FENIB. Human Molecular Genetics *22*, 4616. 10.1093/hmg/ddt310.

74. Wong, M., and Guo, D. (2013). Dendritic spine pathology in epilepsy: Cause or consequence? Neuroscience *251*, 141–150. 10.1016/j.neuroscience.2012.03.048.

75. Xu, X., Miller, E.C., and Pozzo-Miller, L. (2014). Dendritic spine dysgenesis in Rett syndrome. Frontiers in Neuroanatomy *8*.

76. Torres, M.D., Garcia, O., Tang, C., and Busciglio, J. (2018). Dendritic spine pathology and thrombospondin-1 deficits in Down syndrome. Free Radical Biology and Medicine *114*, 10–14. 10.1016/j.freeradbiomed.2017.09.025.

77. Chapleau, C.A., Calfa, G.D., Lane, M.C., Albertson, A.J., Larimore, J.L., Kudo, S., Armstrong, D.L., Percy, A.K., and Pozzo-Miller, L. (2009). Dendritic spine pathologies in hippocampal pyramidal neurons from Rett syndrome brain and after expression of Rett-associated MECP2 mutations. Neurobiology of Disease *35*, 219–233. 10.1016/j.nbd.2009.05.001.

78. Samson, A.L., Nevin, S.T., Croucher, D., Niego, B., Daniel, P.B., Weiss, T.W., Moreno, E., Monard, D., Lawrence, D.A., and Medcalf, R.L. (2008). Tissue-type plasminogen activator requires a co-receptor to enhance NMDA receptor function. J Neurochem *107*, 1091–1101. 10.1111/j.1471-4159.2008.05687.x.

79. Nicole, O., Docagne, F., Ali, C., Margaill, I., Carmeliet, P., MacKenzie, E.T., Vivien, D., and Buisson, A. (2001). The proteolytic activity of tissue-plasminogen activator enhances NMDA receptor-mediated signaling. Nat Med *7*, 59–64. 10.1038/83358.

80. Lebeurrier, N., Liot, G., Lopez-Atalaya, J.P., Orset, C., Fernandez-Monreal, M., Sonderegger, P., Ali, C., and Vivien, D. (2005). The brain-specific tissue-type plasminogen activator inhibitor, neuroserpin, protects neurons against excitotoxicity both in vitro and in vivo. Molecular and Cellular Neuroscience *30*, 552–558. 10.1016/j.mcn.2005.09.005.

81. BBMap (2023). SourceForge. https://sourceforge.net/projects/bbmap/.

82. Dobin, A., Davis, C.A., Schlesinger, F., Drenkow, J., Zaleski, C., Jha, S., Batut, P., Chaisson, M., and Gingeras, T.R. (2013). STAR: ultrafast universal RNA-seq aligner. Bioinformatics *29*, 15–21. 10.1093/bioinformatics/bts635.

83. Liao, Y., Smyth, G.K., and Shi, W. (2014). featureCounts: an efficient general purpose program for assigning sequence reads to genomic features. Bioinformatics *30*, 923–930. 10.1093/bioinformatics/btt656.

84. Pachitariu, M., and Stringer, C. (2022). Cellpose 2.0: how to train your own model. Nat Methods *19*, 1634–1641. 10.1038/s41592-022-01663-4.

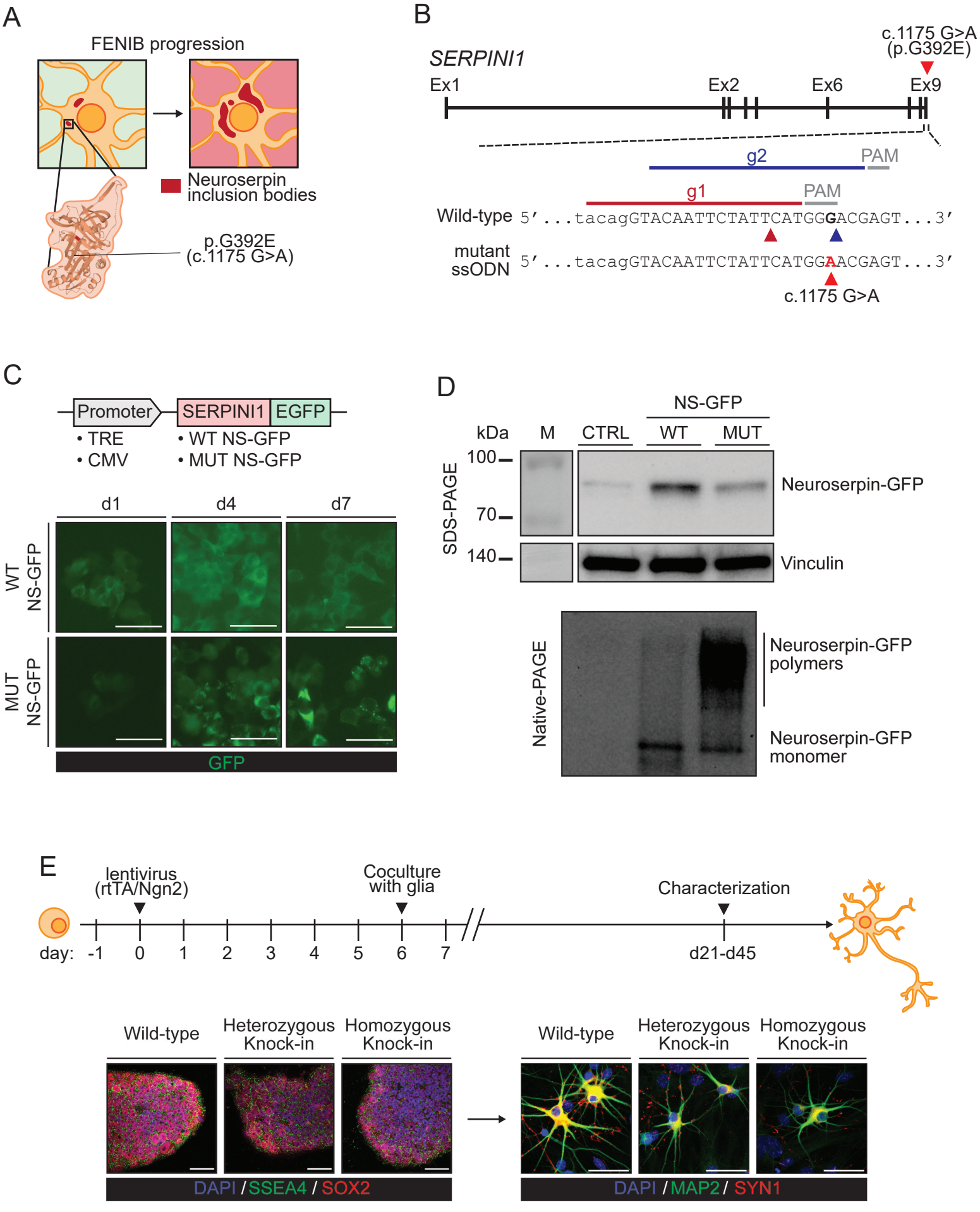
A
FENIB progression
Neuroserpin inclusion bodies
p.G392E (c.1175 G>A)
B
SERPINI1
c.1175 G>A (p.G392E)
Ex1
Ex2
Ex6
Ex9
g2
PAM
g1
PAM
Wild-type 5′...tacagGTACAATTCTATTCATGGGACGAGT...3′
mutant ssODN 5′...tacagGTACAATTCTATTCATGGAACGAGT...3′
c.1175 G>A
C
Promoter
SERPINI1
EGFP
• TRE
• CMV
• WT NS-GFP
• MUT NS-GFP
d1
d4
d7
WT NS-GFP
MUT NS-GFP
GFP
D
NS-GFP
kDa
M
CTRL
WT
MUT
SDS-PAGE
100
70
140
Neuroserpin-GFP
Vinculin
Native-PAGE
Neuroserpin-GFP polymers
Neuroserpin-GFP monomer
E
lentivirus (rtTA/Ngn2)
Coculture with glia
Characterization
day: -1 0 1 2 3 4 5 6 7
d21-d45
Wild-type
Heterozygous Knock-in
Homozygous Knock-in
DAPI / SSEA4 / SOX2
Wild-type
Heterozygous Knock-in
Homozygous Knock-in
DAPI / MAP2 / SYN1

Figure 1

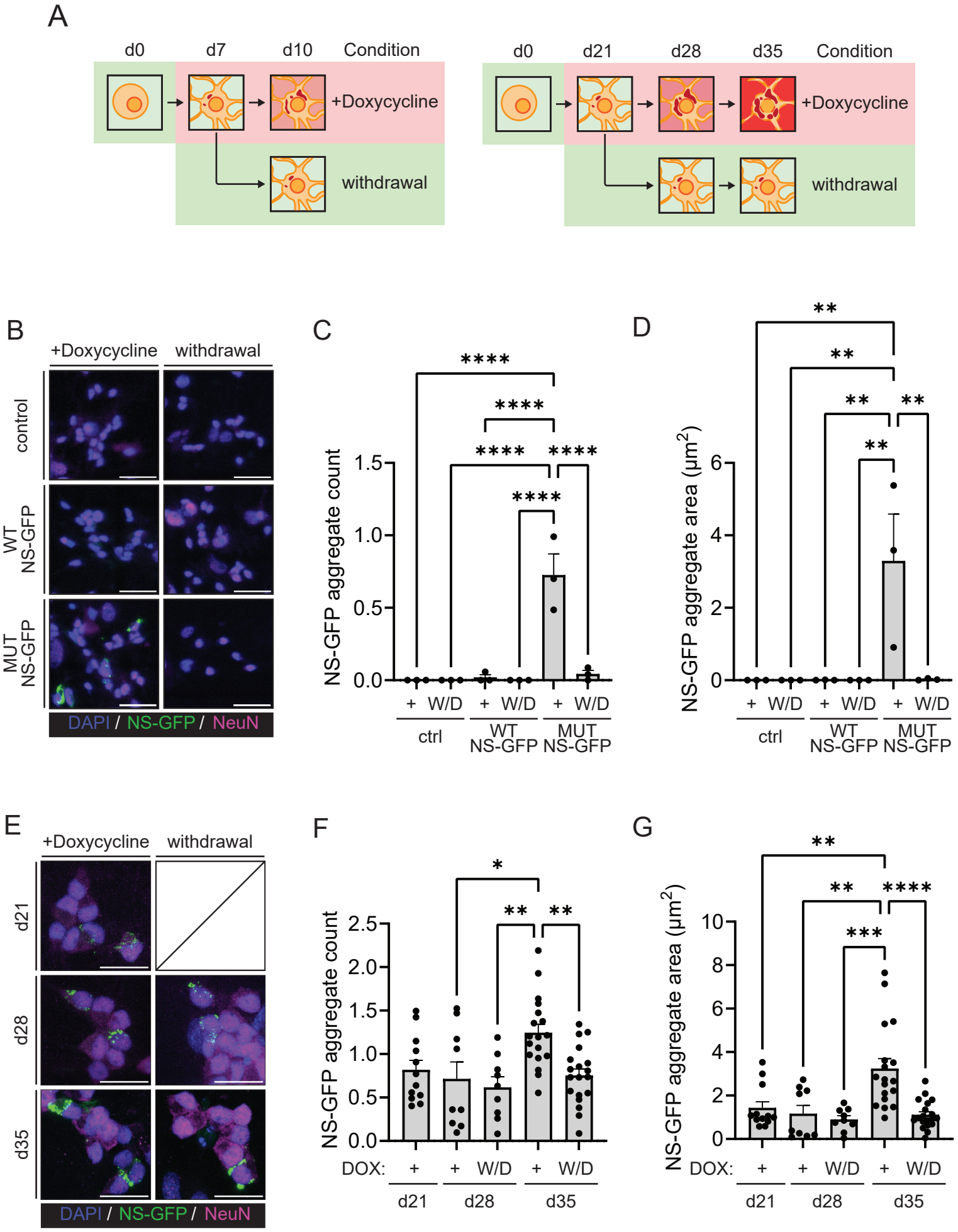
A
d0
d7
d10
Condition
+Doxycycline
withdrawal
d0
d21
d28
d35
Condition
+Doxycycline
withdrawal
B
+Doxycycline
withdrawal
control
WT NS-GFP
MUT NS-GFP
DAPI / NS-GFP / NeuN
C
NS-GFP aggregate count
1.5
1.0
0.5
0.0
****
****
****
****
****
+ W/D + W/D + W/D
ctrl
WT NS-GFP
MUT NS-GFP
D
NS-GFP aggregate area (μm2)
6
4
2
0
**
**
**
**
**
+ W/D + W/D + W/D
ctrl
WT NS-GFP
MUT NS-GFP
E
+Doxycycline
withdrawal
d21
d28
d35
DAPI / NS-GFP / NeuN
F
NS-GFP aggregate count
2.5
2.0
1.5
1.0
0.5
0.0
*
**
**
DOX: + + W/D + W/D
d21
d28
d35
G
NS-GFP aggregate area (μm2)
10
8
6
4
2
0
**
**
****
***
DOX: + + W/D + W/D
d21
d28
d35

Figure 2

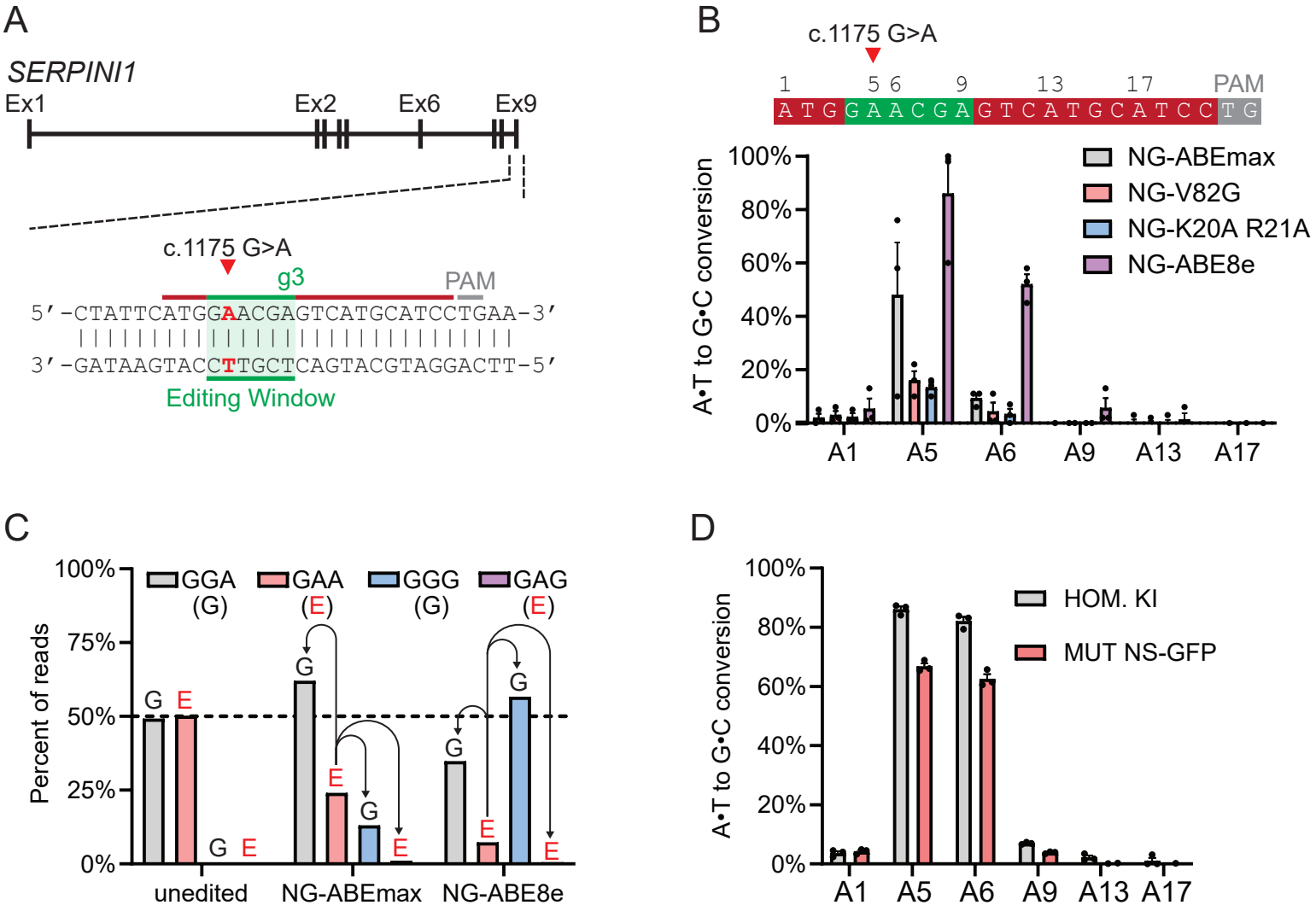
A
SERPINI1
Ex1
Ex2
Ex6
Ex9
c.1175 G>A
g3
PAM
5′-CTATTCATGGAACGAGTCATGCATCCTGAA-3′
3′-GATAAGTACCTTGCTCAGTACGTAGGACTT-5′
Editing Window
B
c.1175 G>A
1 5 6 9 13 17 PAM
ATGGAACGAGTCATGCATCCTG
A•T to G•C conversion
100%
80%
60%
40%
20%
0%
NG-ABEmax
NG-V82G
NG-K20A R21A
NG-ABE8e
A1 A5 A6 A9 A13 A17
C
Percent of reads
100%
75%
50%
25%
0%
GGA (G)
GAA (E)
GGG (G)
GAG (E)
unedited
NG-ABEmax
NG-ABE8e
D
A•T to G•C conversion
100%
80%
60%
40%
20%
0%
HOM. KI
MUT NS-GFP
A1 A5 A6 A9 A13 A17

Figure 3

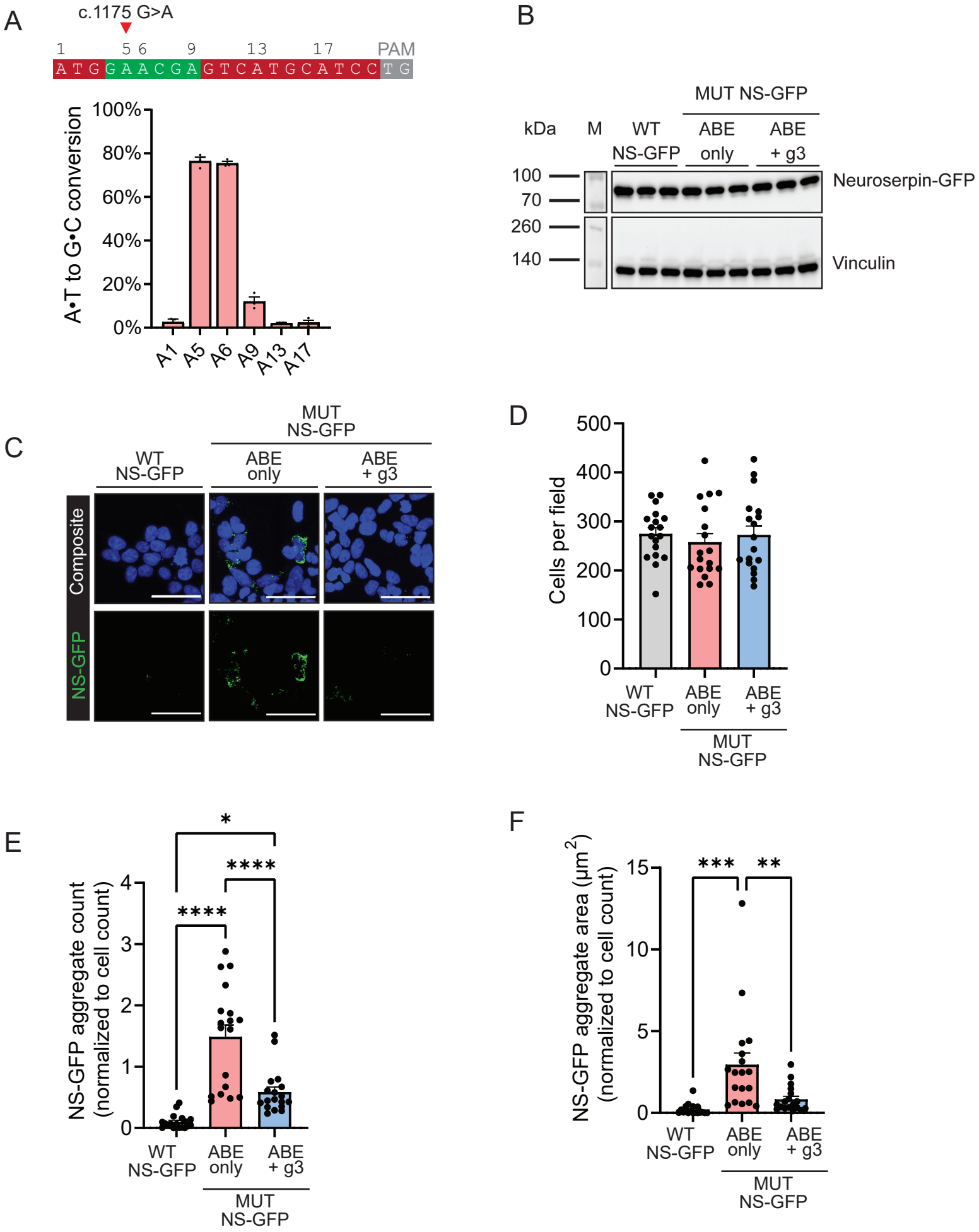
A
c.1175 G>A
1 5 6 9 13 17 PAM
ATGGAACGAGTCATGCATCCTG
A•T to G•C conversion
100%
80%
60%
40%
20%
0%
A1
A5
A6
A9
A13
A17
B
MUT NS-GFP
kDa
M
WT NS-GFP
ABE only
ABE + g3
100
70
260
140
Neuroserpin-GFP
Vinculin
C
MUT NS-GFP
WT NS-GFP
ABE only
ABE + g3
Composite
NS-GFP
D
Cells per field
500
400
300
200
100
0
WT NS-GFP
ABE only
ABE + g3
MUT NS-GFP
E
NS-GFP aggregate count (normalized to cell count)
4
3
2
1
0
*
****
****
WT NS-GFP
ABE only
ABE + g3
MUT NS-GFP
F
NS-GFP aggregate area (μm2) (normalized to cell count)
15
10
5
0
***
**
WT NS-GFP
ABE only
ABE + g3
MUT NS-GFP

Figure 4

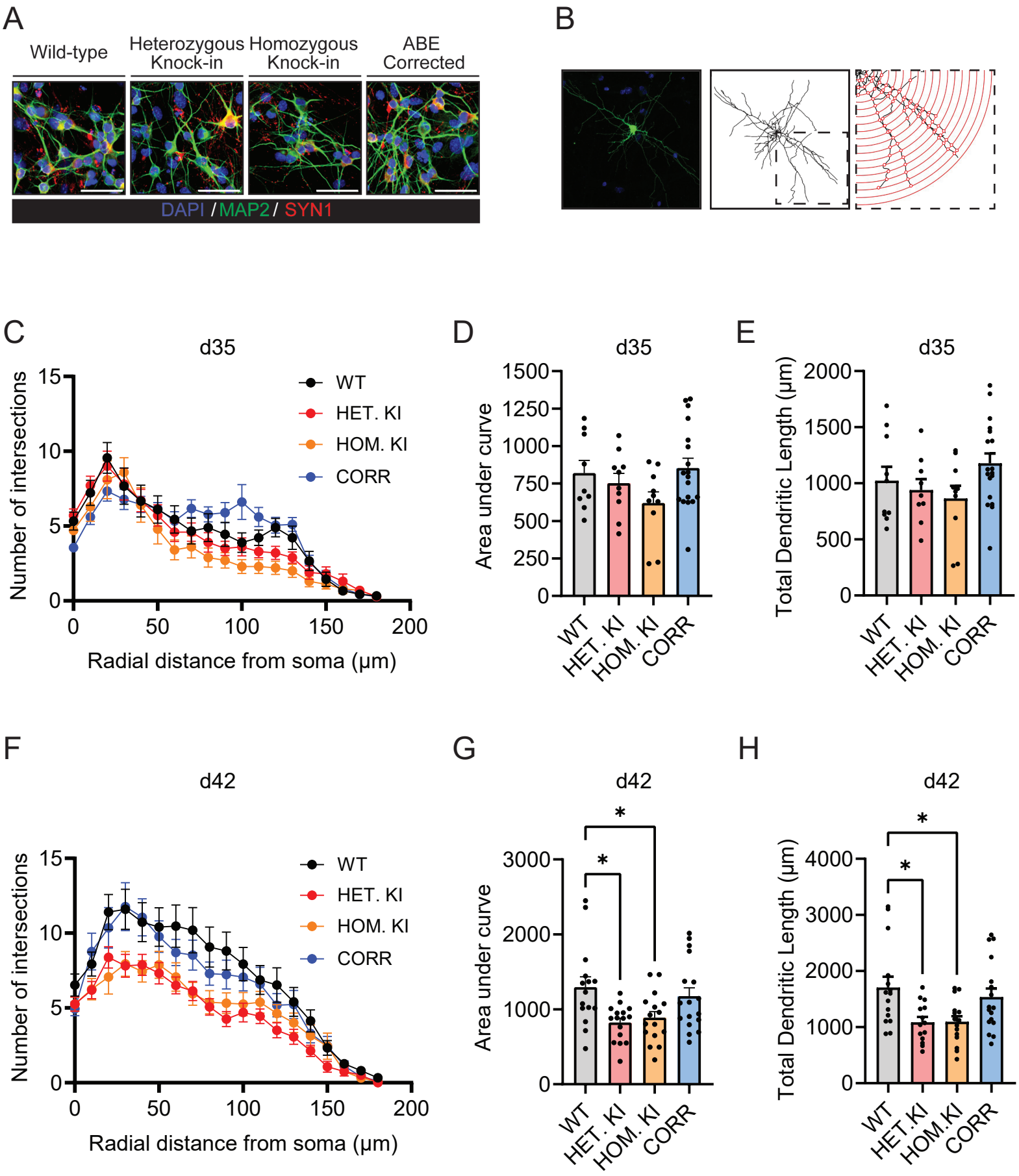
A
Wild-type
Heterozygous Knock-in
Homozygous Knock-in
ABE Corrected
DAPI / MAP2 / SYN1
B
C
d35
Number of intersections
Radial distance from soma (µm)
WT
HET. KI
HOM. KI
CORR
D
d35
Area under curve
WT
HET. KI
HOM. KI
CORR
E
d35
Total Dendritic Length (µm)
WT
HET. KI
HOM. KI
CORR
F
d42
Number of intersections
Radial distance from soma (µm)
WT
HET. KI
HOM. KI
CORR
G
d42
Area under curve
WT
HET. KI
HOM. KI
CORR
H
d42
Total Dendritic Length (µm)
WT
HET.KI
HOM.KI
CORR

Figure 5

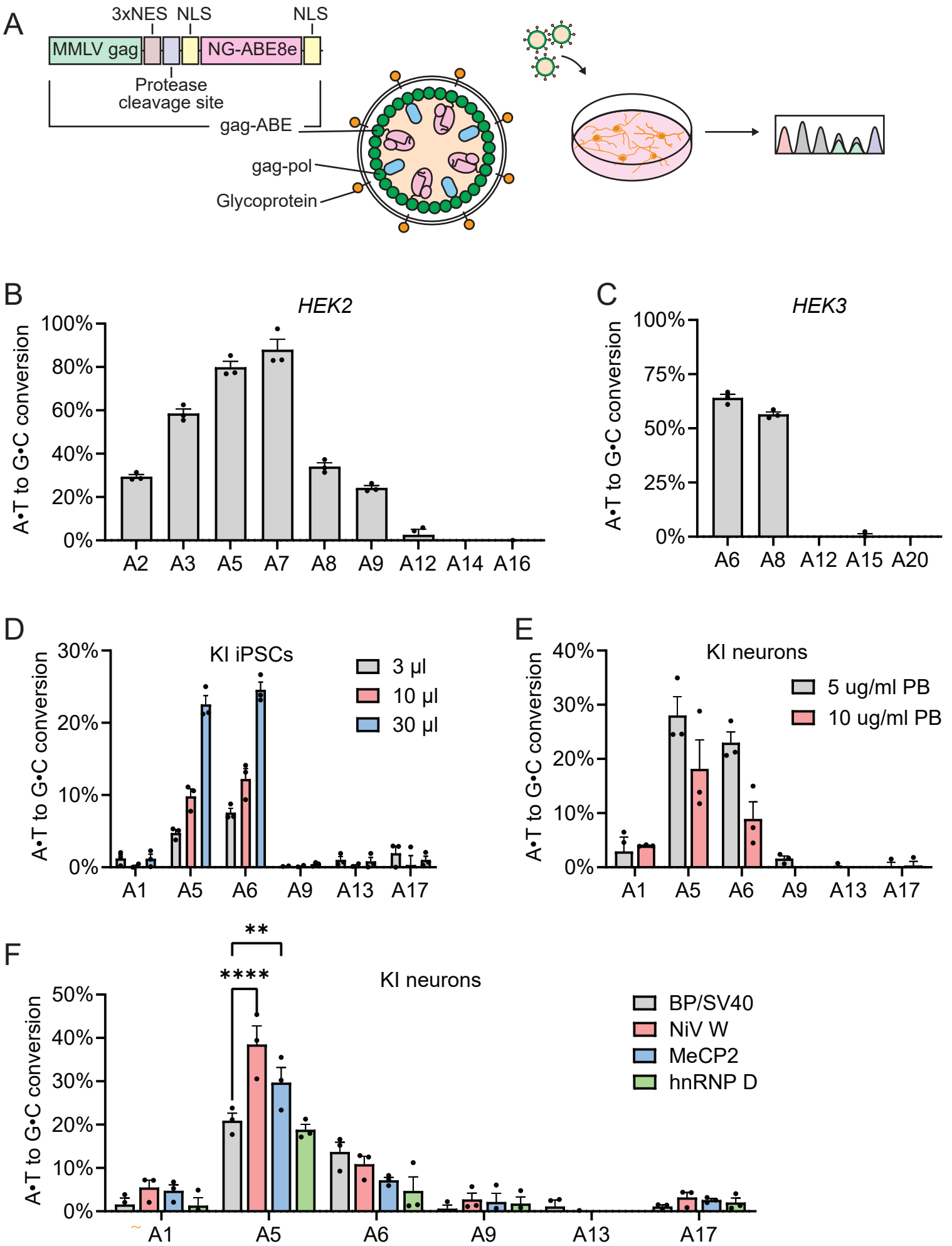
A
3xNES
NLS
NLS
MMLV gag
NG-ABE8e
Protease cleavage site
gag-ABE
gag-pol
Glycoprotein
B
HEK2
A•T to G•C conversion
100%
80%
60%
40%
20%
0%
A2
A3
A5
A7
A8
A9
A12
A14
A16
C
HEK3
A•T to G•C conversion
100%
75%
50%
25%
0%
A6
A8
A12
A15
A20
D
KI iPSCs
3 µl
10 µl
30 µl
A•T to G•C conversion
30%
20%
10%
0%
A1
A5
A6
A9
A13
A17
E
KI neurons
5 ug/ml PB
10 ug/ml PB
A•T to G•C conversion
40%
30%
20%
10%
0%
A1
A5
A6
A9
A13
A17
F
KI neurons
**
****
BP/SV40
NiV W
MeCP2
hnRNP D
A•T to G•C conversion
50%
40%
30%
20%
10%
0%
A1
A5
A6
A9
A13
A17

Figure 6

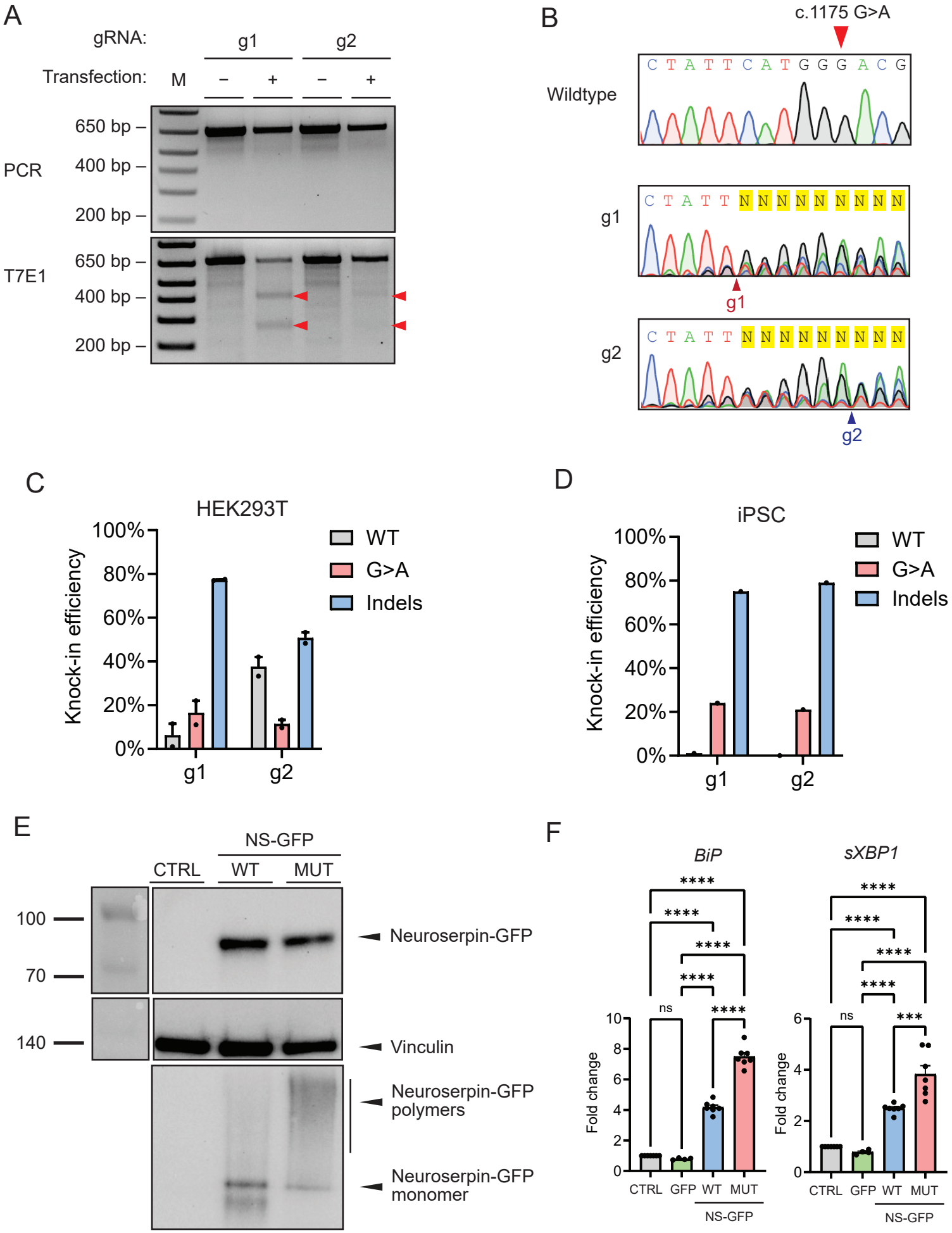
A
gRNA:
g1
g2
Transfection:
M
–
+
–
+
PCR
650 bp
400 bp
200 bp
T7E1
650 bp
400 bp
200 bp
B
c.1175 G>A
Wildtype
C T A T T C A T G G G A C G
g1
C T A T T N N N N N N N N N
g1
g2
C T A T T N N N N N N N N N
g2
C
HEK293T
Knock-in efficiency
100%
80%
60%
40%
20%
0%
WT
G>A
Indels
g1
g2
D
iPSC
Knock-in efficiency
100%
80%
60%
40%
20%
0%
WT
G>A
Indels
g1
g2
E
NS-GFP
CTRL
WT
MUT
100
70
140
Neuroserpin-GFP
Vinculin
Neuroserpin-GFP polymers
Neuroserpin-GFP monomer
F
BiP
sXBP1
****
****
****
****
ns
****
Fold change
10
8
6
4
2
0
CTRL
GFP
WT
MUT
NS-GFP
****
****
****
****
ns
***
Fold change
6
4
2
0
CTRL
GFP
WT
MUT
NS-GFP

Figure S1

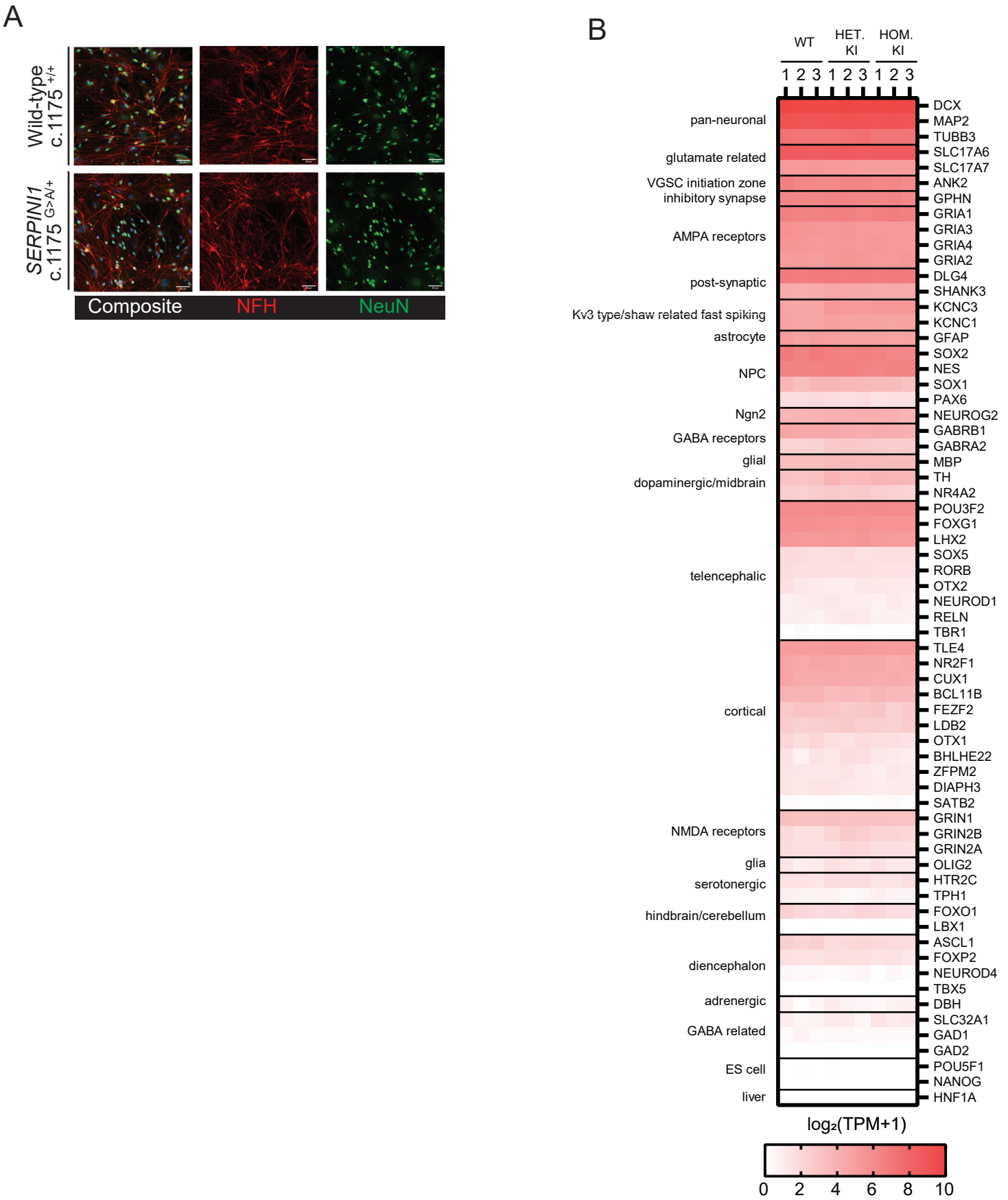
A
Wild-type c.1175 +/+
SERPINI1 c.1175 G>A/+
Composite
NFH
NeuN
B
WT
HET. KI
HOM. KI
1 2 3 1 2 3 1 2 3
pan-neuronal
glutamate related
VGSC initiation zone
inhibitory synapse
AMPA receptors
post-synaptic
Kv3 type/shaw related fast spiking
astrocyte
NPC
Ngn2
GABA receptors
glial
dopaminergic/midbrain
telencephalic
cortical
NMDA receptors
glia
serotonergic
hindbrain/cerebellum
diencephalon
adrenergic
GABA related
ES cell
liver
DCX
MAP2
TUBB3
SLC17A6
SLC17A7
ANK2
GPHN
GRIA1
GRIA3
GRIA4
GRIA2
DLG4
SHANK3
KCNC3
KCNC1
GFAP
SOX2
NES
SOX1
PAX6
NEUROG2
GABRB1
GABRA2
MBP
TH
NR4A2
POU3F2
FOXG1
LHX2
SOX5
RORB
OTX2
NEUROD1
RELN
TBR1
TLE4
NR2F1
CUX1
BCL11B
FEZF2
LDB2
OTX1
BHLHE22
ZFPM2
DIAPH3
SATB2
GRIN1
GRIN2B
GRIN2A
OLIG2
HTR2C
TPH1
FOXO1
LBX1
ASCL1
FOXP2
NEUROD4
TBX5
DBH
SLC32A1
GAD1
GAD2
POU5F1
NANOG
HNF1A
log2(TPM+1)
0 2 4 6 8 10

Figure S2

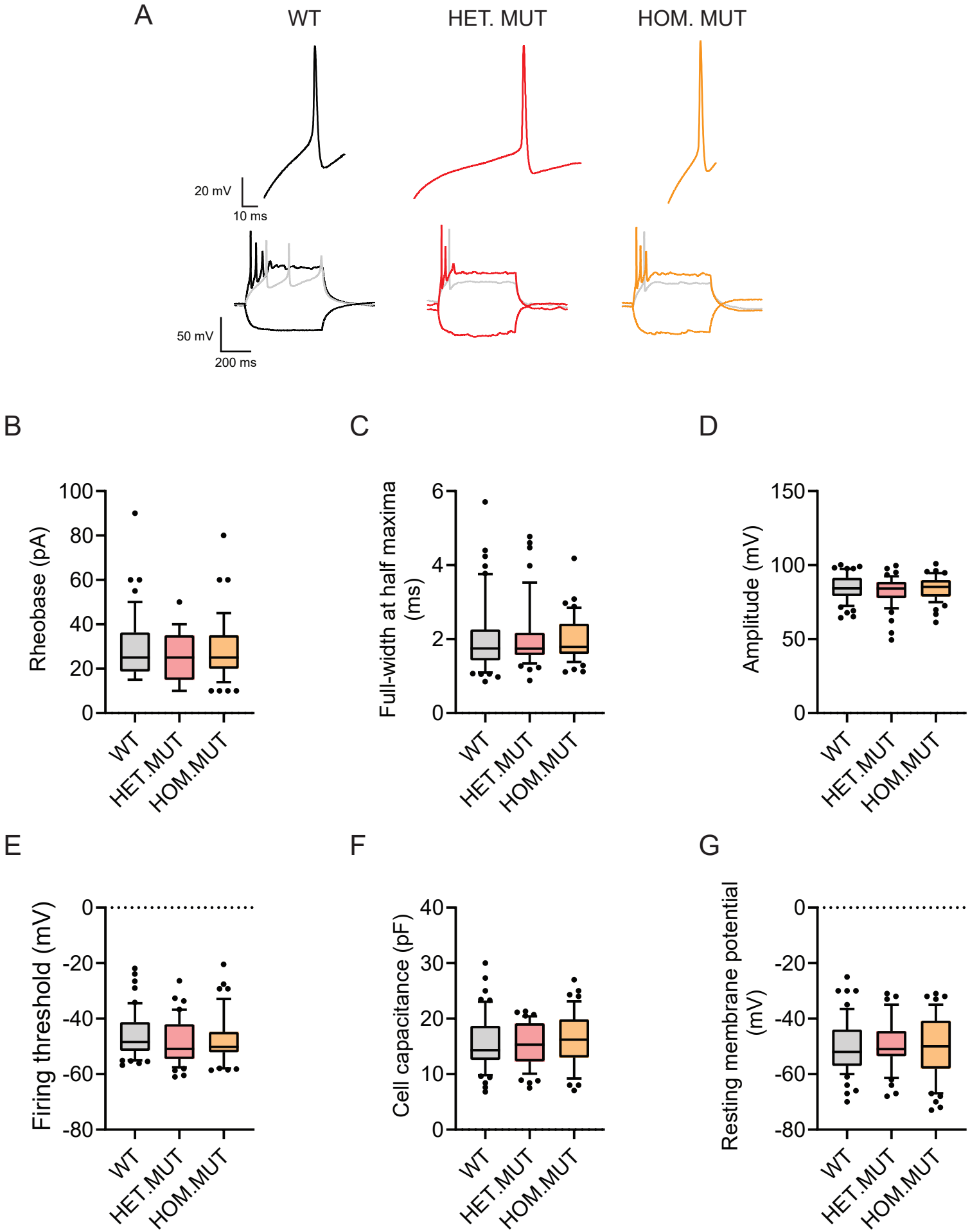
A
WT
HET. MUT
HOM. MUT
20 mV
10 ms
50 mV
200 ms
B
Rheobase (pA)
C
Full-width at half maxima (ms)
D
Amplitude (mV)
E
Firing threshold (mV)
F
Cell capacitance (pF)
G
Resting membrane potential (mV)
WT
HET.MUT
HOM.MUT

Figure S3

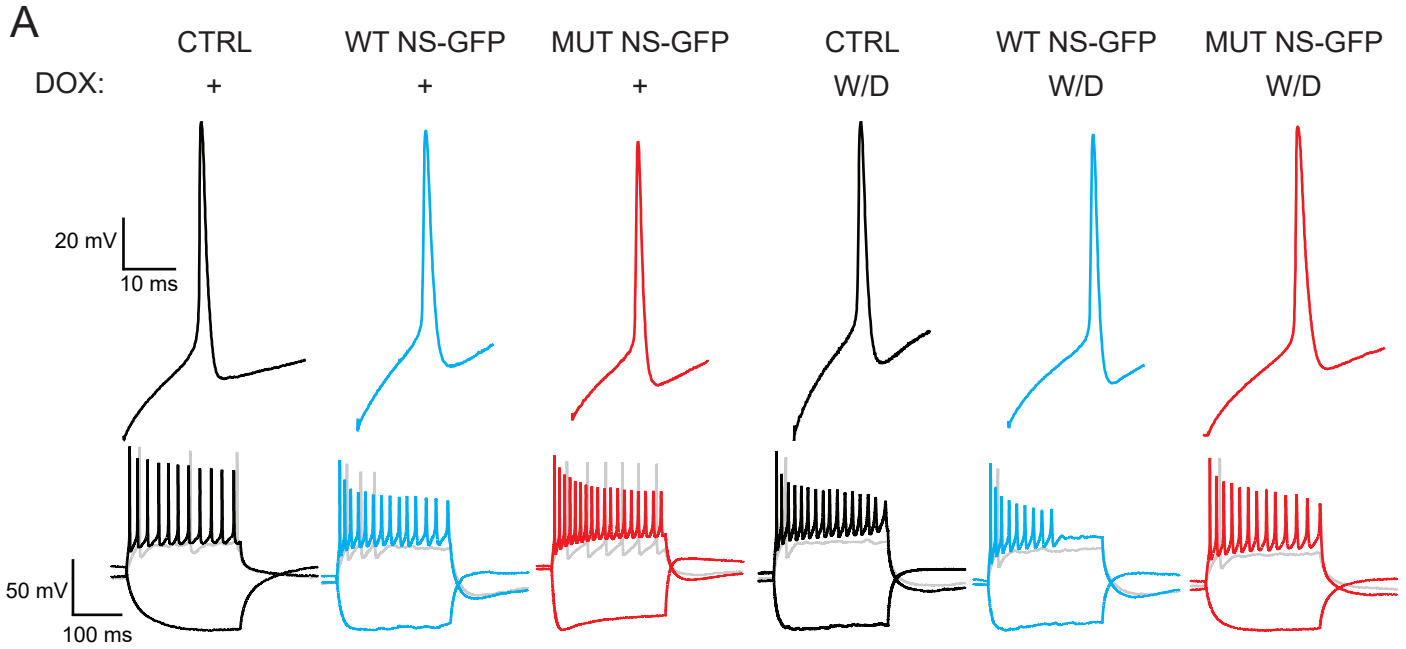
A
CTRL
WT NS-GFP
MUT NS-GFP
CTRL
WT NS-GFP
MUT NS-GFP
DOX:
+
+
+
W/D
W/D
W/D
20 mV
10 ms
50 mV
100 ms

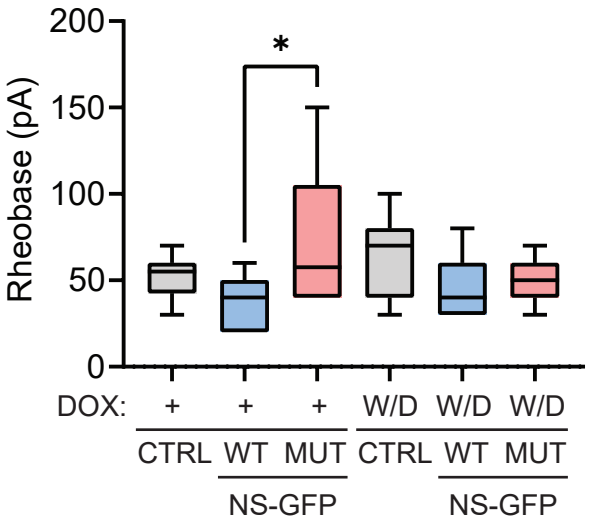
B
Rheobase (pA)
200
150
100
50
0
*
DOX:
+
+
+
W/D
W/D
W/D
CTRL
WT
MUT
CTRL
WT
MUT
NS-GFP
NS-GFP

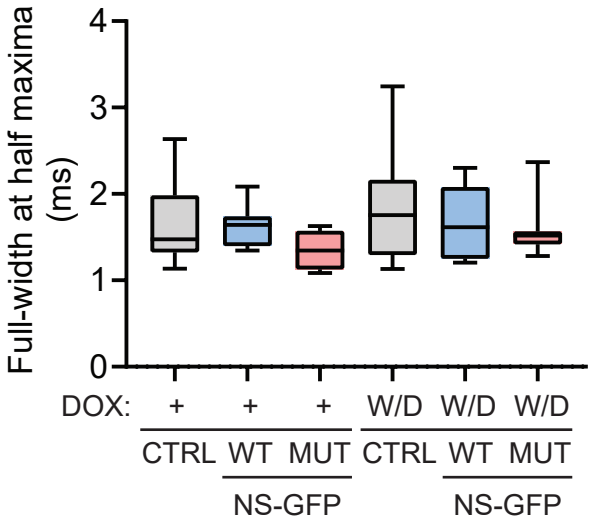
C
Full-width at half maxima (ms)
4
3
2
1
0
DOX:
+
+
+
W/D
W/D
W/D
CTRL
WT
MUT
CTRL
WT
MUT
NS-GFP
NS-GFP

Figure S4

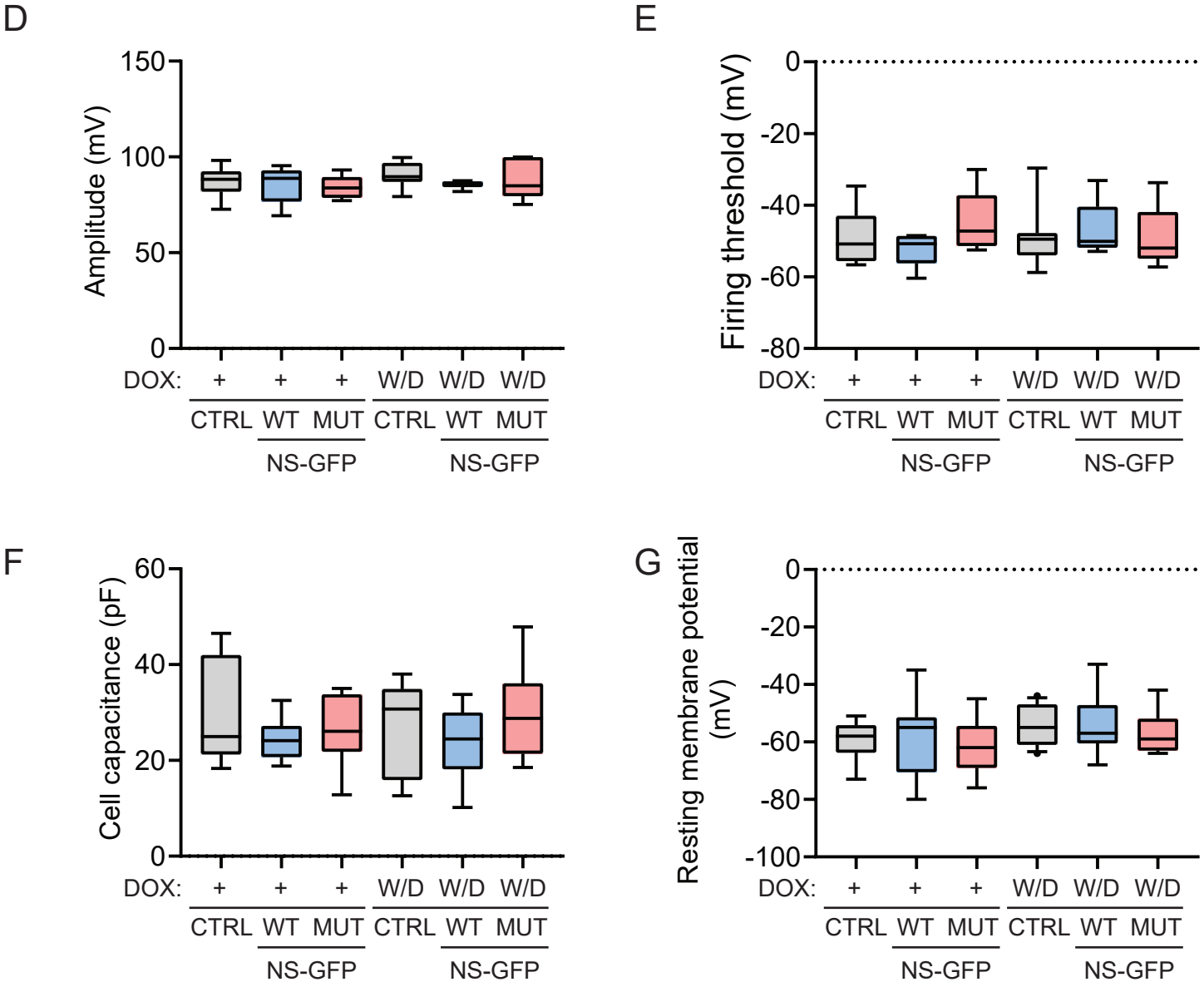
D
Amplitude (mV)
150
100
50
0
DOX: + + + W/D W/D W/D
CTRL WT MUT CTRL WT MUT
NS-GFP NS-GFP
E
Firing threshold (mV)
0
-20
-40
-60
-80
DOX: + + + W/D W/D W/D
CTRL WT MUT CTRL WT MUT
NS-GFP NS-GFP
F
Cell capacitance (pF)
60
40
20
0
DOX: + + + W/D W/D W/D
CTRL WT MUT CTRL WT MUT
NS-GFP NS-GFP
G
Resting membrane potential (mV)
0
-20
-40
-60
-80
-100
DOX: + + + W/D W/D W/D
CTRL WT MUT CTRL WT MUT
NS-GFP NS-GFP

Figure S4

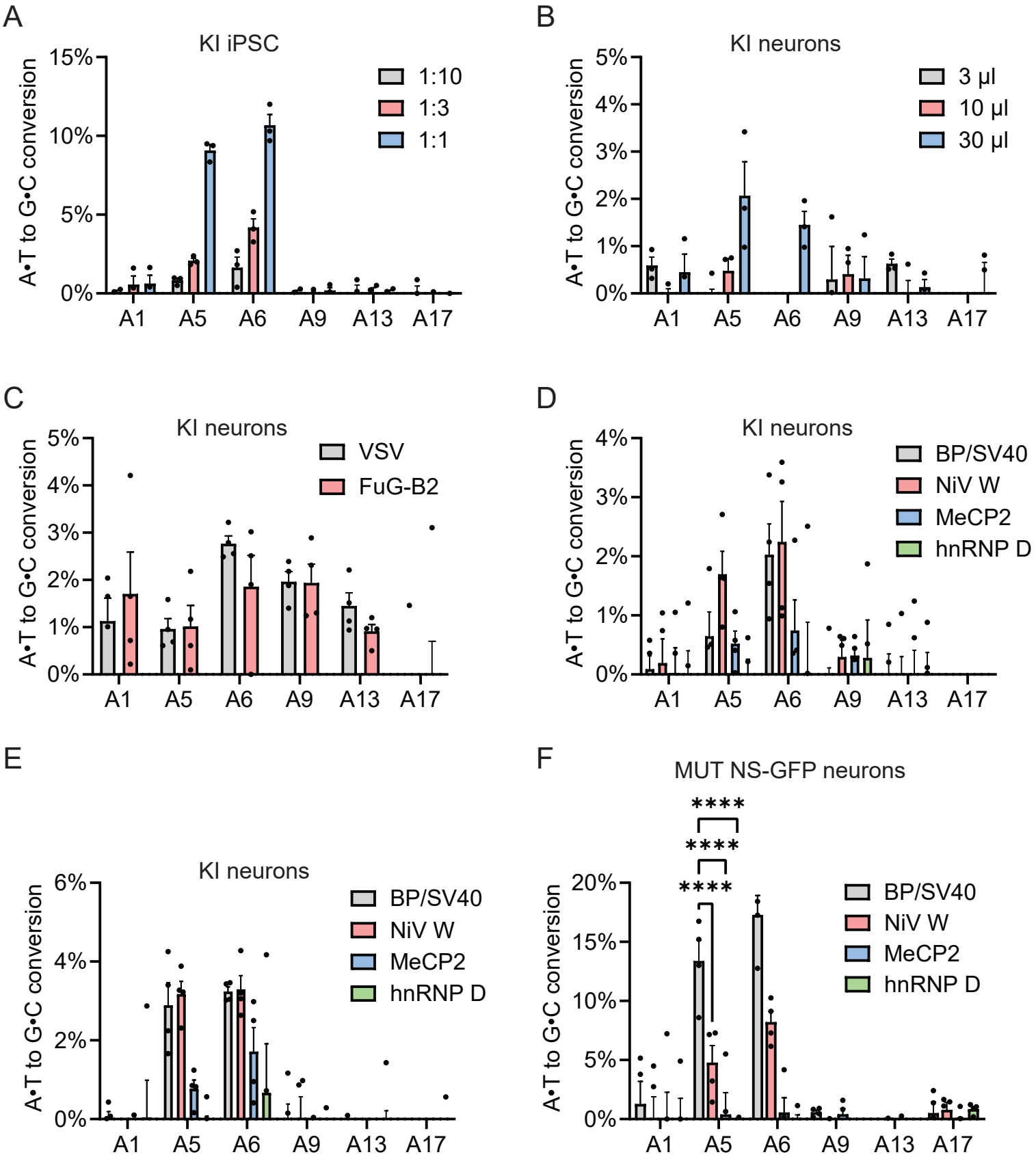
A
KI iPSC
A•T to G•C conversion
15%
10%
5%
0%
1:10
1:3
1:1
A1
A5
A6
A9
A13
A17
B
KI neurons
A•T to G•C conversion
5%
4%
3%
2%
1%
0%
3 µl
10 µl
30 µl
A1
A5
A6
A9
A13
A17
C
KI neurons
A•T to G•C conversion
5%
4%
3%
2%
1%
0%
VSV
FuG-B2
A1
A5
A6
A9
A13
A17
D
KI neurons
A•T to G•C conversion
4%
3%
2%
1%
0%
BP/SV40
NiV W
MeCP2
hnRNP D
A1
A5
A6
A9
A13
A17
E
KI neurons
A•T to G•C conversion
6%
4%
2%
0%
BP/SV40
NiV W
MeCP2
hnRNP D
A1
A5
A6
A9
A13
A17
F
MUT NS-GFP neurons
****
****
****
A•T to G•C conversion
20%
15%
10%
5%
0%
BP/SV40
NiV W
MeCP2
hnRNP D
A1
A5
A6
A9
A13
A17

Figure S5